Large eddy simulation of gas–particle kinematic decoupling and turbulent entrainment in volcanic plumes

Matteo Cerminara[a,b,c,*], Tomaso Esposti Ongaro[a], Augusto Neri[a]

[a] *Istituto Nazionale di Geofisica e Vulcanologia, Section of Pisa – via della Faggiola 32, 56126, Pisa, Italy*
[b] *Scuola Normale Superiore – piazza dei Cavalieri 7, 56126, Pisa, Italy*
[c] *University of Pisa, Department of Mathematics – largo Pontecorvo 5, 56127, Pisa, Italy*

Abstract

In the framework of the IAVCEI (International Association of Volcanology and Chemistry of the Earth Interior) intercomparison study on volcanic plume models, we present three-dimensional (3D) numerical simulations carried out with the ASHEE (ASH Equilibrium Eulerian) model. The ASHEE model solves the compressible balance equations of mass, momentum, and enthalpy of a gas-particle mixture and it is able to describe the kinematic decoupling for particles characterized by Stokes number (i.e., the ratio between the particle equilibrium time and the flow characteristic time) below about 0.2 (or particles smaller than about 1 mm). The computational fluid dynamic model is designed to accurately simulate a turbulent flow field by using a Large Eddy Simulation approach, and it is thus suited to analyze the role of particle non-equilibrium in the dynamics of turbulent volcanic plumes. The two reference scenarios analyzed correspond to a weak (mass eruption rate $=1.5 * 10^6$ kg/s) and a strong volcanic plume (mass eruption rate $= 1.5 * 10^9$ kg/s) in absence of wind. For each scenario, we compare the 3D results, averaged in space and time, with theoretical results obtained from integral plume models. Such an approach allows to quantitatively evaluate the effects of grid resolution and subgrid-scale turbulence model, and the influence of gas-particle non-equilibrium processes on the large-scale plume dynamics. We thus demonstrate that the uncertainty on the numerical solution associated with such effects can be significant (of the order of 20%), but still lower than that typically associated with input data and integral model approximations. In the Weak Plume case, 3D results are consistent with the predictions of integral models in the jet and plume regions, with an entrainment coefficient around 0.10 in the plume region. In the Strong Plume case, the self-similarity assumption is less appropriate and the entrainment coefficient in the plume region is more unstable, with an average value of 0.24. For both cases, integral models predictions diverge from the 3D plume behavior in the umbrella region. The presented analysis of 3D numerical simulations thus allows to identify the critical hypotheses at the base of integral models used in operational studies. In addition, high-resolution 3D runs allow to reproduce observables quantities (such as infrasound signals) which can be useful to constrain eruption dynamics in real cases.

Keywords: volcanic plumes, large eddy simulations, dispersed multiphase turbulence, entrainment coefficient, grain size distribution, numerical model

---

[*] Corresponding author
Email address: `matteo.cerminara@gmail.com` (Matteo Cerminara)
URL: `https://sites.google.com/site/matteocerminara/` (Matteo Cerminara)

2010 MSC: 86-02, 86-04, 86-08, 86A10, 76-02, 76-04, 76F25, 76F45, 76F50, 76F65, 76H05, 76T15, 76T20, 76T30, 35Q30, 35Q86, 34-02, 34E05

---

1. Introduction

Volcanic plumes are characterized by the injection in the atmosphere of a high-velocity, high-temperature mixture of gases and pyroclasts of different densities and sizes, mostly in the range from a few tens of microns to several millimeters. The dynamics of volcanic columns are largely governed by turbulence, which controls air entrainment, heating and expansion, and the consequent transition from a momentum-driven jet to a positively buoyant plume or to a collapsing fountain (Sparks et al., 1997). Despite the advancement of the computational capability and the improvement of the measurement techniques in the laboratory, turbulence still is one of the least understood scientific problems. One major difficulty, of course, is that the governing equations of fluid dynamics are nonlinear and little is known about their solutions at high Reynolds number, even in simple geometries and for an ideal fluid. This picture is even more complicated when a dispersed solid phase is added to the turbulent flows, as occurring in volcanic plumes.

Nonetheless, the need of providing interpreting models for volcanic observations and hazard forecast tools makes it urgent to develop and assess the quality and reliability of volcanic plume models. To this aim, IAVCEI (the International Association of Volcanology and Chemistry of the Earth Interior) has promoted the volcanic plume model inter-comparison study, a systematic effort to compare different models performing a set of simulations using the same input parameters (Costa et al., 2016; Suzuki et al., 2016). These represent a weak (mass eruption rate $=1.5 * 10^6$ kg/s) and strong (m.e.r.$=1.5 * 10^9$ kg/s) volcanic plume in a stratified atmosphere. Input data were set assuming source conditions and atmospheric profiles representative, respectively, of the 26 January 2011 Shinmoe-dake eruption (Suzuki and Koyaguchi, 2013) and the 15 June 1991 Pinatubo eruption (see, e.g. Holasek et al., 1996). In this framework we have developed the present study, by just considering plume development in windless conditions.

One-dimensional (1D) models based on various developments of the Morton et al. (1956) buoyant plume theory (we refer to them as *integral* or *1D* models) have been extremely useful in volcanology mainly because they have allowed to correlate the observed (or reconstructed) column height with the mass eruption rate, which is usually extremely difficult to measure directly (Wilson et al., 1980; Sparks, 1986). On the other hand, integral models are routinely used in hazard assessment studies and whenever there is the need of computationally efficient tools to forecast volcanic plume heights, e.g. for atmospheric ash dispersal models (most of such 1D tools are reviewed by Costa et al., 2016, this issue). Unfortunately, such models are extremely sensitive to the choice of their main empirical parameter, the entrainment coefficient. The entrainment coefficient expresses empirically a proportionality between the rate of air entrainment at a given height and the average plume vertical velocity. It is usually calibrated from controlled experiments at the laboratory scale. The dominant control of the entrainment coefficient on integral model results is demonstrated, inter alia, by the analysis presented by de' Michieli Vitturi et al. (2016) in the framework of the same intercomparison study. A significant portion of the early and even more recent literature on volcanic plume models has thus been devoted to identifying, by means of experimental or theoretical studies, the right, or better value of the entrainment coefficient, sometimes expressed as a function of height, density contrast or Richardson number (Kaminski et al., 2005; Carazzo et al., 2008; Woods, 2010).

To overcome this difficulty, computational fluid dynamics bypasses the shortcomings of analytical methods and integral numerical models by offering Direct Numerical Simulations (DNS), i.e., the simulation of the whole range of spatial and temporal scales in the turbulent flow. With respect to other investigation methods, DNS is more akin to an experiment, and no less valuable for the immense quantity of data it produces. Unfortunately, as demonstrated in Sect. 2, the DNS of volcanic plumes is presently computationally unaffordable, because it would require an extremely fine numerical grid. The main idea behind the Large Eddy Simulation (LES) approach adopted in this work is to reduce this computational cost by reducing the range of time- and length-scales that are being solved for via a low-pass filtering of the equations. Such a low-pass filtering effectively removes small-scale information from the numerical solution. However, nonlinearity causes the coupling between the large and the small scales, introducing subgrid-scale (SGS) terms that cannot in general be disregarded (Vreman et al., 1995). To mimic the SGS effect on the large scales, reproducing correctly the resolved turbulent spectrum, SGS models take advantage of the universal character of turbulence at the smallest scales.

In turbulent plumes, experimental and numerical studies (see e.g., da Silva et al., 2014, for a review) support the idea that the *rate* of air entrainment is controlled by the dynamics of the large eddies, at the so-called Taylor microscale (see Sect. 2). It is therefore necessary to understand to what extent LES is suited to describe turbulent plumes and how important the unresolved SGS part of the turbulent spectrum (which must be modeled) can be of practical volcanological interest. The first objective of this work is therefore to quantify the sensitivity to grid resolution of three-dimensional (3D) LES of a volcanic plume model and to provide an empirical quantitative estimate of the minimum grid size required to minimize the effect of the modeled subgrid turbulence.

Just a few authors (Suzuki et al., 2005; Esposti Ongaro et al., 2008; Herzog and Graf, 2010; Cerminara et al., 2016), in the last ten years, have envisaged the 3D LES of volcanic columns (such 3D models are reviewed by Suzuki et al., 2016). Their works have allowed to explore the influence of more realistic vent conditions on eruption dynamics and to put further constraints on semi-empirical parameters needed by integral models, in particular, the entrainment coefficient (Suzuki and Koyaguchi, 2010), also in presence of wind or water microphysics (Suzuki and Koyaguchi, 2015; Van Eaton et al., 2015). The ASHEE (Ash Equilibrium Eulerian) model adopted in this work and described in Sect. 3 has been recently developed (Cerminara et al., 2016) to accurately simulate the spectral properties of dispersed multiphase turbulence for particles smaller than about 1 mm.

ASHEE is implemented to describe mean (i.e. plume shape and height) and fluctuation (i.e. turbulent infrasound) properties of volcanic plumes, and the effects of kinematic decoupling on the dynamics of turbulent gas–particle mixtures. It is indeed widely accepted that the structure of turbulent flows can be largely affected by the presence of solid particles (e.g., Elghobashi, 1991, 1994; Toschi and Bodenschatz, 2009). Because of their inertia, particles tend to preferentially concentrate in the regions of low shear (Balachandar and Eaton, 2010), thus creating large clusters which can eventually modify the eddy structure. How this phenomenon affects the turbulent mixing at the interface with the ambient fluid is still an open question. In this work, we address the problem by comparing LES of turbulent volcanic plumes carried out with and without including the effects of particle decoupling.

The buoyant plume theory provides a valuable tool to get insight into 3D simulation results, and it is therefore complementary to LES. We introduce in Appendix C two integral models: a new formulation (ASH1D) of the 1D plume model proposed by Woods (1988), and its zero-dimensional asymptotic approximation for dilute regimes (ASH0D). A methodology to coherently compare time- and space-averaged 3D simulations and integral model outcomes is introduced in Sect. 3.4. Comparison between ASHEE, ASH1D and ASH0D results in Sect. 4 and Sect. 5 allows to critically revise the hypotheses at the base of 1D models and, in particular, to discuss the entrainment hypothesis and the value of the entrainment coefficient which can be derived from 3D numerical models.

2. Time and length scales of volcanic plumes

Turbulence is a multiscale physical phenomenon involving many different scales, from the integral scale of the flow to the scale of the smallest eddy of the turbulent field. The turbulent entrainment process at the interface between two regions at different turbulent intensity (such as the boundary between the plume and the atmosphere) is carried out through two different mechanisms: large-scale eddies are responsible of the engulfment of parcels of air (Townsend, 1966), whereas small-scale turbulence controls the so-called nibbling process (Mathew and Basu, 2002; Bisset et al., 2002). Although experimental studies (Westerweel et al., 2005) suggest that the nibbling process controls the development of the turbulent/non-turbulent interface, it is still believed that the global rate of entrainment is imposed by the large-scale engulfment (e.g., Taveira et al., 2011; da Silva et al., 2014).

The smallest scale in a volcanic plume is given by the Kolmogorov scale (Pope, 2000)

$$\eta = A_\eta D \mathrm{Re}^{-\frac{3}{4}} \, . \tag{1}$$

Here, D is the vent diameter, A_η is a constant depending on the geometry of the problem and $\mathrm{Re} = DU/\nu$ is the Reynolds number based on the flow properties at the vent (U is the vent velocity and ν is the kinematic viscosity). Plourde et al. (2008) estimated $A_\eta \simeq 5.6$ for a pure plume. The Kolmogorov characteristic time scale of the smallest eddies is $\tau_\eta = \eta^2/\nu$. In volcanic eruptions, the order of magnitude of the Kolmogorov microscales typically is $\eta \approx 10\,\mu\mathrm{m}$ and $\tau_\eta \approx 10\,\mu\mathrm{s}$.

The order of magnitude of the integral scale for the plume development is the plume height. This can be estimated as a function of the steady release of thermal energy at the crater $\dot{Q}_\mathrm{W} = \rho_\mathrm{m} U \pi (D/2)^2 C_\beta (T_\beta - T_\alpha)$, by means of the following formula:

$$H_\mathrm{top} = A_\mathrm{W}\, \dot{Q}_\mathrm{W}^{\frac{1}{4}} \, , \tag{2}$$

where C_β and T_β are the specific heat at constant pressure and the temperature of the ejected mixture, respectively, while T_α is the surrounding atmosphere temperature. Wilson et al. (1978) estimated $A_{\mathrm{W}} \simeq 8.2$ for volcanic plumes.

When Re is high (in volcanic plumes it typically ranges in $10^6 \div 10^{10}$) the integral and the Kolmogorov scales are separated by many orders of magnitude (cf. Eq. (1)). Between these two scales there exists the so called inertial sub-range, where the turbulent properties of the flow are universal and do not depend on the integral scale configuration. This sub-range is characterized by the Taylor microscale λ_{T}. Because λ_{T} depends on the flow configuration, it is difficult to estimate it a-priori. In Sects. 4 and 5, we will compute this length scale *a-posteriori* from the results of 3D simulations.

The temporal integral scale t_{top} can be evaluated thanks to Morton et al. (1956). It depends only on atmospheric parameters:

$$t_{\mathrm{top}} \simeq \sqrt{\frac{T_1}{g\Gamma(1+n)}}\,, \tag{3}$$

where Γ is the atmospheric adiabatic lapse rate, T_1 is the atmospheric temperature at the vent level and n is the ratio of the vertical temperature gradient to the lapse rate Γ. In standard atmospheric conditions ($\Gamma = 9.8\,\mathsf{K/km}$ and $n = -0.66$), we obtain $t_{\mathrm{top}} \simeq 100\,\mathsf{s}$. We recall that this time scale depends only on atmospheric parameters because the only temporal scale in stratified self-similar plumes is the Brunt-Väisällä frequency (through the gravity acceleration).

2.1. Degrees of freedom of volcanic plumes

On the basis of the scaling analysis above, we are able to estimate the number of degrees of freedom to be resolved to fully simulate a turbulent volcanic plume in a DNS. The order of magnitude of the number of spatial and temporal degrees of freedom can be given by

$$N_{\mathrm{spatial}} \approx \left(\frac{H_{\mathrm{top}}}{\eta}\right)^3 \tag{4}$$

$$N_{\mathrm{temporal}} = \frac{t_{\mathrm{top}}}{\tau_\eta}\,. \tag{5}$$

Thus, the number of degrees of freedom to be resolved in a volcanic simulation is:

$$\begin{aligned} N_{\mathrm{d.o.f.}} = N_{\mathrm{spatial}} N_{\mathrm{temporal}} &= \frac{t_{\mathrm{top}} H_{\mathrm{top}}^3 U}{A_\eta^5 D^4} \mathrm{Re}^{\frac{11}{4}} = \\ &= \frac{t_{\mathrm{top}} A_{\mathrm{W}}^3 (\rho_{\mathrm{m}} C_\beta (T_\beta - T_\alpha))^{\frac{3}{4}}}{A_\eta^5} \frac{U^{\frac{9}{2}} D^{\frac{1}{4}}}{\nu^{\frac{11}{4}}}\,. \end{aligned} \tag{6}$$

Setting the typical values for a volcanic eruption (cf. Wilson et al., 1978) to $(T_\beta - T_\alpha) = 1000\,\mathsf{K}$, $\rho_{\mathrm{m}} = 5\,\mathsf{kg/m^3}$, $C_\beta = 1100\,\mathsf{J/(K\,kg)}$ and $\nu \simeq 2 * 10^{-5}\,\mathsf{m^2/s}$, we obtain (in SI unit):

$$N_{\mathrm{d.o.f.}} = 9.5 * 10^{19} * U^{\frac{9}{2}} D^{\frac{1}{4}}\,, \tag{7}$$

which is huge, even for small volcanic eruptions. The LES approach has been developed to mitigate this unaffordable computational effort. This approach takes advantage of the fact that in a fully turbulent flow the vast majority of modes is below the Taylor microscale (Pope, 2000). In the LES approach this small scales (far from the integral scales) are modeled by assuming that the spectrum has an universal shape. This approach has been demonstrated to be accurate if the resolved scales ξ are in the inertial range.

For a volcanic plume, it has been numerically observed that the grid resolution at the vent must be at least $\xi \simeq D/10$ (cf. i.e., Zhou et al., 2001; Suzuki et al., 2005) to approach the inertial sub-range. Therefore, we can recount the number of degrees of freedom for a volcanic LES by using $D/10$ as smallest spatial scale and $D/(10U)$ as smallest temporal scale (instead of the Kolmogorov scales). We obtain:

$$N_{\mathrm{d.o.f.}} = 10^4\,\frac{t_{\mathrm{top}} H_{\mathrm{top}}^3 U}{D^4} = 10^4\,\frac{t_{\mathrm{top}} A_{\mathrm{W}}^3 (\rho_{\mathrm{m}} C_\beta (T_\beta - T_\alpha))^{\frac{3}{4}} U^{\frac{7}{4}}}{D^{\frac{5}{2}}}\,, \tag{8}$$

or, using the typical values for a volcanic eruption (in SI unit):

$$N_{\mathrm{d.o.f.}} = 6.3 * 10^{14} * U^{\frac{7}{4}} D^{-\frac{5}{2}}\,. \tag{9}$$

It is worth noting here that, contrary to intuition, larger plumes are less expensive to model than small ones. For example, a Plinian eruption can have $D \simeq 1000\,\mathsf{m}$ and $U \simeq 300\,\mathsf{m/s}$, bringing to $N_{\mathrm{d.o.f.}} \simeq 4.3 * 10^{11}$ while a Strombolian with $D \simeq 10\,\mathsf{m}$ and $U \simeq 10\,\mathsf{m/s}$ brings to $N_{\mathrm{d.o.f.}} = 1.1 * 10^{14}$. Even if these numbers are still very large, they could be mitigated by using non-homogeneous grid geometries, because Re is not homogeneous in the domain. In Sects. 4 and 5, we use the ASHEE model for the LES of two volcanic plumes.

3. Model description

The ASHEE model is a multiphase fluid dynamic model conceived for mixtures composed by I gaseous components and J particulate phases of solid particles. To identify the I gaseous components we use the index i, while j runs over the J solid phases. We use the index k for a generic phase or component in the mixture. All the phases are treated using the Eulerian approach, identifying a particle phase as a class of particles with similar dynamical properties (size, density, shape and specific heat). In this section we review the model, which has been presented in more detail by Cerminara et al. (2016) and Cerminara (2016). Numerical benchmarks demonstrating the quality and reliability of DNS and LES of turbulent flows are also discussed by Cerminara et al. (2016).

3.1. Physical model

The physical model behind ASHEE is a generalization of the dusty-gas ([dusty], also known as pseudo-gas) model by Marble (1970).

In the [dusty] model, the gas–particle mixture at position $\boldsymbol{x} \in \Omega$ and time $t \in \mathcal{T}$ is characterized by the following Eulerian fields: 1) the mixture density ρ_{m}; 2) the gas and solid mass fractions y_i and y_j respectively; 3) the mixture velocity $\boldsymbol{u}_{\mathrm{m}}$; 4) the mixture enthalpy h_{m}. The peculiarity of the [dusty] model with respect to full multiphase models is the local equilibrium assumption between all the phases. In other words, all the phases are assumed to be in kinematic ($\boldsymbol{u}_i = \boldsymbol{u}_j = \boldsymbol{u}_{\mathrm{m}}$) and thermal ($T_i = T_j = T$) equilibrium.

The non-dimensional number measuring the degree of disequilibrium between a particle class and the carrier gas phase is the Stokes number St (Balachandar and Eaton, 2010). It compares the typical equilibrium time of a solid particle (the Stokes time τ_{s}) with the fastest time of the dynamical process under analysis. In Cerminara et al. (2016) we show that St relative to kinematic and thermal disequilibrium are of the same order of magnitude for volcanic ash. The [dusty] model is well suited for solving multiphase mixtures if $\mathrm{St} < 10^{-3}$ (Balachandar and Eaton, 2010) for all the evolution of the dynamical process under analysis. If the particle size increases the Stokes number increases, making the disequilibrium between the gas and the particles more important. In volcanic plumes, two main processes arise because of the kinematic decoupling: 1) particle settling; 2) preferential concentration. The first phenomenon is the fallout of ash particles from the volcanic plume due to gravity acceleration and the density contrast between ash and gas phases. The second is the tendency of heavy particles to escape from turbulence eddies because of centrifugal acceleration. The ASHEE model uses the equilibrium–Eulerian [eqEu] model (Ferry and Balachandar, 2001) instead of [dusty], in order to extend its validity up to $\mathrm{St} \simeq 0.2$ for the preferential concentration and to ash size $d_{\mathrm{s}} \simeq 1\,\mathsf{mm}$ for the settling of ash in the atmosphere (Cerminara, 2016). As we discuss in more detail in the following, the Stokes number does not depend only on the properties of the particles but also on the typical time of the dynamics. In turbulent flows, the dynamics is characterized by the coexistence of a wide range of temporal and spatial scales (eddies). Thus, St is different for each eddy scale ξ, and in particular it is larger for smaller eddies ($\mathrm{St} \propto \xi^{-2/3}$, Balachandar and Eaton, 2010). Consequently, disequilibrium is more important at smaller scales. However, as we discuss in the next section, typically in turbulence most of the energy is transported by large eddies (characterized by the Taylor microscale λ_{T}). Therefore we will focus our analysis on disequilibrium at these scales.

Besides the hypothesis on the Stokes number, ASHEE (as well as the dusty-gas model) only considers the dilute regime. Elghobashi (1991, 1994) characterized the dilute regime on the basis of the volumetric concentration of solid particles in the mixture:

$$\epsilon_{\mathrm{s}} = \frac{\sum_j V_j}{V} \lesssim 10^{-3}\,. \tag{10}$$

In such a dilute limit, different coupling regimes can be described. In the *two-way* coupling regime, the mutual effects of the carrier fluid and particles are considered, but interactions among particles are disregarded. The regime in which all the possible interactions are taken into account is called *four-way* coupling. In the present work, we are taking into account the effect of the particles on the gas phase because the mass fraction of the solid phase is not small. Indeed, in volcanic plumes, even if ϵ_{s} is small, the density contrast between the ash and gas phase is large. Defining $\hat{\rho}_{\mathrm{g}}$ and $\hat{\rho}_{\mathrm{s}}$ the density of the gas and solid phase respectively, and ρ_{g} and ρ_{s} their bulk densities, we have $\hat{\rho}_{\mathrm{s}}/\hat{\rho}_{\mathrm{g}} \approx 10^3$, thus the bulk density of the solid phase can be of the same order of that of the gas phase:

$$\rho_{\mathrm{s}} = \epsilon_{\mathrm{s}}\hat{\rho}_{\mathrm{s}} \lesssim \hat{\rho}_{\mathrm{g}} \simeq (1-\epsilon_{\mathrm{s}})\hat{\rho}_{\mathrm{g}} = \epsilon_{\mathrm{g}}\hat{\rho}_{\mathrm{g}} = \rho_{\mathrm{g}}\,. \tag{11}$$

We recall here that the mixture density is defined as the sum of the bulk densities of all the components and phases:

$$\rho_\mathrm{m} \equiv \rho_\mathrm{g} + \rho_\mathrm{s} = \sum_i \rho_i + \sum_j \rho_j \,, \tag{12}$$

and that the mass fractions are defined as:

$$y_i = \frac{\rho_i}{\rho_\mathrm{m}} \,, \qquad y_j = \frac{\rho_j}{\rho_\mathrm{m}} \,, \qquad \sum_i y_i + \sum_j y_j = 1 \,. \tag{13}$$

We refer to a generic field $\mathfrak{f}$ as associated to the gas components $\mathfrak{f}_i$, to the solid phases $\mathfrak{f}_j$ and to the mixture $\mathfrak{f}_\mathrm{m} = \sum_i y_i \mathfrak{f}_i + \sum_j y_j \mathfrak{f}_j$. In other words, a quantity referred to the mixture is its mass weighted average over all the components and phases.

The equations used in the ASHEE model are reported in Appendix B. Additional details can be found in Cerminara et al. (2016) and Cerminara (2016).

3.2. Subgrid-scale models

In ASHEE the spatial-scales below the grid scale are modeled using the LES approach for compressible flows. In this approach, the model (B.1) is spatially-filtered to separate the resolved scales from the subgrid scales. The contribution of the subgrid scales endures in the model because of the presence of non-linear terms. These terms can be modeled using the Boussinesq eddy viscosity hypothesis and the eddy diffusivity viscosity model (e.g., Garnier et al., 2009). Eddy diffusivity models require that a few SGS coefficients are provided as a function of the resolved variables. These are the eddy viscosity μ_t, the SGS kinetic energy K_t and Prandtl number Pr_t. We refer to Erlebacher et al. (1990); Moin et al. (1991); Garnier et al. (2009); Cerminara et al. (2016) for a description of the adopted LES approach. While our SGS models do not explicitly depend on the spatial coordinate or direction, it is worth remarking that non-isotropic formulations might be adopted in which eddy viscosity coefficients depend explicitly on the position (see, e.g. Costa et al., 2006).

We have tested several state-of-the-art SGS models, both static and dynamic (for which we present numerical benchmarks in Cerminara et al., 2016; Cerminara, 2016). Dynamic models are preferable with respect to static ones because they do not require to evaluate the SGS coefficients empirically. Instead, they are calculated locally, on the basis of the resolved turbulent spectrum. This procedure is preferable even in presence of non-homogeneous LES dynamics and boundary conditions. In this work we present results obtained with: the dynamic WALE model [dynWale] (see Nicoud and Ducros, 1999; Lodato et al., 2009; Piscaglia et al., 2013); the dynamic Smagorinsky model [moin] in the form by Moin et al. (1991); the static SGS K-equation model [oneEqEddy] (see Chacón Rebollo and Lewandowski, 2013; Fureby, 1996; Yoshizawa, 1993; Chai and Mahesh, 2012). This allows us to assess the influence of SGS Reynolds stresses on simulation results. Finally, we also performed simulations without SGS model [noM].

3.3. Numerical solver

The Eulerian model described in Sect. 3 and detailed in Appendix B is solved numerically to obtain a time-dependent description of all independent flow fields in a 3D domain with prescribed initial and boundary conditions. Spatial discretization is achieved by means of a Finite Volumes approach on an unstructured mesh. In the present application, the spatial gradients are discretized by adopting an unlimited centered linear scheme (which is second-order accurate and has low *numerical diffusion* – Ferziger and Perić, 1996; Cerminara et al., 2016). Analogously, implicit advective fluxes at the control volume interfaces are reconstructed by using a centered linear interpolation scheme (also second order accurate). The only exception is for pressure fluxes in the pressure correction equation, for which we adopt a TVD (Total Variation Diminishing) limited linear scheme (in the subsonic regimes) to enforce stability and non-oscillatory behavior of the solution.

The temporal discretization is based on the second-order Crank-Nicolson scheme (Ferziger and Perić, 1996), with a blending factor of 0.5 (0 meaning a first-order Euler scheme, 1 a second-order, bounded implicit scheme) and an adaptive time step based on the maximum Courant number ($\mathrm{Co} < 0.2$). All advection terms of the model are treated implicitly to enforce stability. Diffusion terms are also discretized implicit in time, with the exception of those representing subgrid turbulence. The pressure and gravity terms in the momentum equations and the continuity equations are solved explicitly, as well as the enthalpy equation.

The system of the Eulerian transport equations is solved by adopting a segregated approach and adopting the PISO algorithm (Pressure Implicit with Splitting of Operators, Issa (1986)). The PISO algorithm consists of one predictor step, where an intermediate velocity field is solved using pressure from the previous time-step, and of a number of PISO corrector steps, where intermediate and final velocity and pressure fields are obtained iteratively. By means of PISO, the pressure and the kinematic non-equilibrium terms are made implicit, thus enforcing the stability of the solution. The segregated system is iteratively solved to make implicit also the enthalpy and the subgrid terms.

The numerical code ASHEE is based on the `C++` libraries OpenFOAM® for solving the compressible balance equations of mass, momentum and enthalpy of the mixture. For a complete description of the numerical algorithm and the structure of the numerical solver, please refer to Cerminara et al. (2016) and references therein.

3.4. Time and space averages

A 1D integral model describing the evolution with height (i.e., along the $\hat{z}$ direction) of the fluxes of mass (πQ), momentum (πM) and enthalpy (πF) in volcanic plumes is presented in Appendix C. Its results are discussed, in the framework of the plume model intercomparison study, by Costa et al. (2016) (this issue). In this section, we describe the procedure to coherently compare integral and 3D model results by integrating the latter in time and space.

Given $\Omega \times \mathcal{T}$, the space-time domain, we first average over $\mathcal{T}$ a generic 3D variable $\mathfrak{f}(\boldsymbol{x}, t)$:

$$\bar{\mathfrak{f}} = \int_{\mathcal{T}} \mathfrak{f}(\boldsymbol{x}, t)\, \mathrm{d}t\,. \tag{14}$$

For every plane Ω_z orthogonal to $\hat{z}$ at height z, we define a plume subset $\mathcal{O}(z) \subset \Omega_z$, defined by the points where the mixture velocity has positive vertical component and the mass fraction of a tracer $\bar{y}_{\mathrm{tracer}}$ is larger than a threshold

y_{min}:

$$\mathcal{O} = \{(x_1, x_2) \in \Omega_z \mid \quad \bar{\boldsymbol{u}}_{\mathrm{m}} \cdot \hat{z} \geq 0 \quad \text{and} \quad \bar{y}_{\mathrm{tracer}} \geq y_{\mathrm{min}}\} \,. \tag{15}$$

We refer to the integral over this domain as:

$$\mathfrak{F}(z) = \langle \bar{\mathfrak{f}}(\boldsymbol{x}) \rangle_{\mathcal{O}} \equiv \int_{\mathcal{O}} \mathrm{d}x_1 \mathrm{d}x_2 \, \bar{\mathfrak{f}}(x_1, x_2, z) \,. \tag{16}$$

In particular, we define the integral mass flux, the kth generic species mass flux, the momentum flux and the enthalpy flux (a modified version of the buoyancy flux taking into account the presence of the different gas and solid species) as follows:

$$\pi Q = \langle \bar{\rho}_{\mathrm{m}} \, \bar{\boldsymbol{u}}_{\mathrm{m}} \cdot \hat{z} \rangle_{\mathcal{O}} \equiv \pi \beta U b^2 \tag{17a}$$

$$\pi Q_k = \langle \bar{\rho}_{\mathrm{m}} \bar{y}_k \, \bar{\boldsymbol{u}}_{\mathrm{m}} \cdot \hat{z} \rangle_{\mathcal{O}} \equiv \pi \beta Y_k U b^2 \tag{17b}$$

$$\pi M = \left\langle \bar{\rho}_{\mathrm{m}} (\bar{\boldsymbol{u}}_{\mathrm{m}} \cdot \hat{z})^2 \right\rangle_{\mathcal{O}} \equiv \pi \beta U^2 b^2 \tag{17c}$$

$$\pi F = \left\langle \left(\frac{1 + \sum_k (\chi_k - 1) \bar{y}_k}{1 + \sum_k (\psi_k - 1) \bar{y}_k} \, \bar{\rho}_\alpha - \bar{\rho}_{\mathrm{m}} \right) (\bar{\boldsymbol{u}}_{\mathrm{m}} \cdot \hat{z}) \right\rangle_{\mathcal{O}} \equiv$$

$$\equiv \pi \left(\frac{1 + Y_\chi}{1 + Y_\psi} \alpha - \beta \right) U b^2 \,, \tag{17d}$$

where $\psi_k = R_k / R_\alpha$ ($\psi_k = 0$ for the solid species) is the gas constant relative to the atmosphere, $\chi_k = C_k / C_\alpha$ is the specific heat at constant pressure relative to the atmosphere, $Y_\psi = \sum_k (\psi_k - 1) Y_k$, $Y_\chi = \sum_k (\chi_k - 1) Y_k$, and $\alpha(z) = \langle \bar{\rho}_\alpha(\boldsymbol{x}) \rangle_{\mathcal{O}}$.

This method allows to compute the time and space averages consistently with the integral description of 1D models and independently from any assumption about the horizontal plume profile (e.g., Gaussian or flat). A similar approach has been adopted by Kaminski et al. (2005) in the Boussinesq approximation, i.e., for small density contrasts.

By defining $Q_\psi = Y_\psi Q$ and $Q_\chi = Y_\chi Q$, we can compute the *integral equivalent* plume variables by using the inversion formulas of Eqs. 17:

$$b(z) = \sqrt{\frac{Q(F + Q)(Q + Q_\psi)}{\alpha M (Q + Q_\chi)}} \tag{18a}$$

$$\beta(z) = \alpha \, \frac{Q(Q + Q_\chi)}{(F + Q)(Q + Q_\psi)} \tag{18b}$$

$$Y_k(z) = \frac{Q_k}{Q} \tag{18c}$$

$$T_\beta(z) = T_\alpha \, \frac{F + Q}{Q + Q_\chi} \tag{18d}$$

$$U(z) = \frac{M}{Q} \,, \tag{18e}$$

where $b(z)$ is the radius, $\beta(z)$ the density, $Y_k(z)$ the mass fraction of a gas or solid species, $T_\beta(z)$ the temperature, $U(z)$ the vertical velocity of the plume as a function of the height above the inlet and $T_\alpha = p / R_\alpha \alpha$ is the atmospheric temperature profile. Finally, the entrainment coefficient can be calculated, from its definition, as:

$$\varkappa(z) = \frac{Q'}{2 \alpha U b} \,, \tag{19}$$

Vent parameter	WP	SP	Units
D	54	1406	m
U_0	135	275	m/s
$T_{\alpha,0}$	270.92	294.66	K
$T_{\beta,0}$	1273	1053	K
α_0	1.11	1.01	kg/m^3
β_0	4.87	3.51	kg/m^3
R_α	287	287	m^2/(s^2 K)
C_α	1004	1004	m^2/(s^2 K)
C_s	1100	1100	m^2/(s^2 K)
g	9.80665	9.80665	m/s^2
d_coarse	1	0.5	mm
d_fine	0.0625	0.016	mm
$\hat{\rho}_\mathrm{coarse}$	2200	2500	kg/m^3
$\hat{\rho}_\mathrm{fine}$	2700	2700	kg/m^3
y_coarse	0.485	0.475	-
y_fine	0.485	0.475	-
y_H2O	0.03	0.05	-
vent elevation	1500	1500	m
lower atmospheric layer	$1500 \div 14317.2$	$1500 \div 14889.1$	m
upper atmospheric layer	$14317.2 \div 20000$	$14889.1 \div 50000$	m
lower thermal gradient	-0.00461	-0.00661	K/m
upper thermal gradient	0.00001	0.00252	K/m

Table 1: Volcanic plume parameters used in this paper.

where $(\cdot)'$ is the derivative along the plume axis. This expression implicitly includes all the mixing processes eventually occurring into the plume, and in particular partial collapse, fallout and re-entrainment.

It is worth noting that the methodology described in this section allows us to coherently compare results obtained from integral models with those obtained from 3D simulations. Moreover, the entrainment coefficient $\varkappa$ – the key empirical parameter for integral models – can be easily obtained for 3D fields. In Sects. 4 and 5 (as well as in Costa et al., 2016; Suzuki et al., 2016), we use this averaging procedure for post-processing 3D plume simulations.

4. Weak plume

The set of input data for the weak plume simulation is discussed in the companion paper by Costa et al. (2016). In this work we have limited our analysis to the windless scenario. In Tab. 1, we report the boundary and initial conditions for the weak (WP) and strong plume (SP) simulations. In particular, the WP case represents a sub-Plinian scenario with mass eruption rate $\pi Q_0 = 1.5 * 10^6$ kg/s. Two particle classes have been used for the simulations, whose features are also reported in Tab. 1. For such particles, the Stokes number can be calculated by taking, as a reference time scale, the typical eddy turnover time at the vent. In analogy with laboratory plumes, this is $\tau_D \sim \mathrm{Str}\frac{D}{U_0} \approx 0.12\,\mathrm{s}$, where D and U_0 are the plume diameter and velocity at the vent, respectively, and Str is the Strouhal number, of the order $\mathrm{Str} = 0.3$ (Zhou et al., 2001). Based on this time scale, and computing the particle relaxation time from Eq. B.13, the Stokes number for the two adopted particle classes in the WP case is about $\mathrm{St}_{\mathrm{coarse}} \approx 5$ and $\mathrm{St}_{\mathrm{fine}} \approx 0.2$. Thus, we expect to see non-equilibrium phenomena for both particles classes, with more evident effects on the coarsest phase. However, the Stokes number, as an average value in the whole plume, is not as high as above. Indeed, by using the spatial-averaged Taylor microscale as reference time for the turbulent dynamics, we obtain $\mathrm{St}_{\mathrm{coarse}} \approx 0.1$ and $\mathrm{St}_{\mathrm{fine}} \approx 0.005$. This result has been obtained *a posteriori*, for the finer mesh resolution, having $\xi \approx 40\,\mathsf{m}$, $K \approx 218\,\mathsf{m}^2/\mathsf{s}^2$ and $\lambda_{\mathrm{T}} \approx 231\,\mathsf{m}$, when the plume reaches its maximum height.

4.1. Large Eddy Simulation results

The computational domain is extended $483b_0 \times 765b_0$ in the radial and vertical directions (b_0 being the vent radius). The numerical grid is non-uniform and non-orthogonal. For the highest resolution run (high-res), the cell size increases from a minimum grid size $\delta = D/32$ with no radial grading factor in the region where the plume is expected to develop, whose initial radius is equal to $2.5b_0$ and increases linearly with an angle θ such that $\tan\theta = 0.147$. Outside this region, a radial grading factor of 1.0446 is applied. Along z, 2048 cells are utilized. The minimum vertical cell size is $\delta = D/32$, and a grading factor of 1.00187 is imposed. The azimuthal resolution is constant and equal to $\frac{1}{32}\pi$ (5.625 degrees). The resulting total number of cells is $10,747,904$. We performed also simulations with the same mesh topology but at lower resolution: mid-res ($\delta = D/16$) and low-res ($\delta = D/8$).

Numerical simulation of $720\,\mathsf{s}$ of eruption required: $34\,\mathsf{h}$ for the low-res case (on one Intel-I7 quad-core processor at 2.8GHz); 10 days for the mid-res case (on 4 AMD 16-core processors at 2.3GHz); 25 days for the high-res case (on 1024 cores of the CINECA IBM BG/Q machine).

Large scale dynamics. Fig. 1 shows the development of the volcanic plume at $t = 400\,\mathsf{s}$. Because of the atmospheric stratification, the plume reaches a neutral buoyancy condition at about $z = H_{\mathrm{nbl}} = 10\,\mathsf{km}$ above the vent (i.e., $11.5\,\mathsf{km}$ above the sea level, still within the troposphere). Due to its inertia, the plume reaches its maximum plume height $H_{\mathrm{top}} \simeq 12\,\mathsf{km}$, before spreading radially to form the so-called volcanic umbrella. The two orthogonal sections highlight the different spatial distribution of the volumetric fraction of fine (right) and coarse (left) ash particles, due to the different coupling regime with the gas phase. Coarse particles have indeed a larger settling velocity $\boldsymbol{w}_s = \tau_s \boldsymbol{g}$ which causes a more intense proximal fallout from the plume margins and a reduced transport by the umbrella. This is highlighted by the plot of the streamlines of the mixture velocity along a vertical section (Fig. 2), showing that the plume updraft is surrounded by a shell of settling coarse particles, which also inhibits air entrainment while promoting particle re-entrainment into the plume.

Kinematic non-equilibrium effects. Besides settling, the large inertia of the coarse ash is responsible for the kinematic decoupling, leading to preferential concentration and clustering of particles at the margins of turbulent eddies. To illustrate this phenomenon, in a non-homogeneous flow, the instantaneous

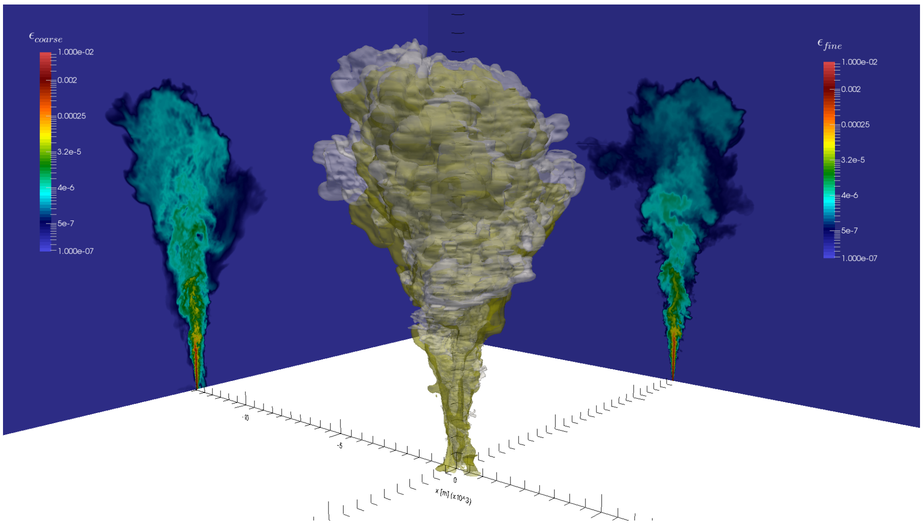

Figure 1: 3D numerical simulation of the WP case, 400 s after the beginning of the eruption (initial conditions as in Tab. 1). The two isosurfaces in 3D rendering correspond to the threshold $\epsilon_s = 10^{-7}$ of the fine (light white) and coarse (light sand) ash volume fractions. The maximum height of the fine class isosurface is approximatively 12.1 km. The two-dimensional plots represent the distribution of the volume concentration of coarse (left) and fine (right) particles across vertical orthogonal slices crossing the plume axis. See color palette for volume concentration values.

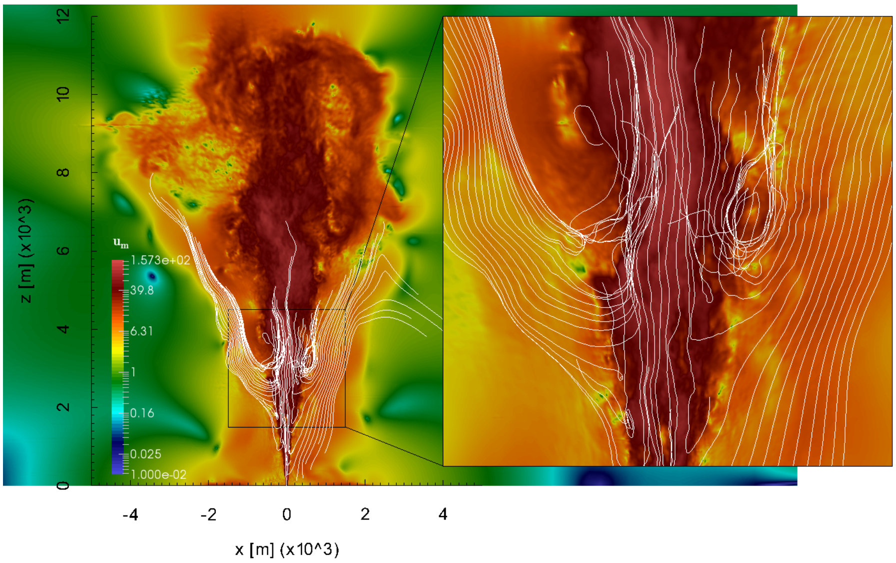

Figure 2: Vertical section of the instantaneous value of the mixture velocity modulus (in logarithmic scale) at $t = 400$ s and velocity streamlines.

preferential concentration is computed as the (normalized) ratio between the jth particle concentration and the concentration of a tracer (in our case, water vapor), i.e.,

$$\mathcal{C}_j = \frac{y_j}{y_{j,0}} \cdot \frac{y_{\mathrm{tracer},0}}{y_{\mathrm{tracer}}} \,, \tag{20}$$

where the 0 subscript corresponds to the value at the vent.

Fig. 3a shows the distribution of $\mathcal{C}_j$ for the coarsest particles at $t = 400\,\mathsf{s}$. The color scale is logarithmic and symmetric with respect to 1, which corresponds to the nil preferential concentration. For $\mathcal{C}_j < 1$, the mixture is relatively depleted of particles (green to blue scale); for $\mathcal{C}_j > 1$, particles are clustered (green to red scale). The mass fraction of the coarsest particles is up to 5 times larger (red zones) and 20 times smaller (blue zones) than the value it would have in absence of preferential concentration (green zones). This behavior affects the mixing and entrainment process, as it will be shown in the following sections, where the mean plume properties are evaluated with and without gas–particle kinematic decoupling (see Figs. 4f, 4g, 4h and associated comments). It is also worth remarking that the more uniform red area beyond the plume margins corresponds to the region of settling particles below the incipient umbrella region, that starts to develop on the left hand-side of the domain in Fig. 3a. On the other hand, the top of the plume is relatively depleted of coarse particles. The corresponding Fig. 3b for fine particles confirms that these are tightly coupled to the gas phase and almost behave as tracers (value of $\mathcal{C}_{\mathrm{fine}}$ is everywhere around 1). These conclusions are coherent with the *a-priori* estimate of St_j we gave at the beginning of this section, based on the Taylor microscale time.

The instantaneous properties that we have just discussed in the plume region are similar for all the subsequent temporal evolution of the plume, provided that the source conditions are kept stationary. As the plume evolves, the umbrella cloud develops horizontally while the particles settle down reaching the ground as ruled by their terminal velocity in the atmosphere.

4.2. Mean properties

We here present the results obtained by averaging the 3D results over time. We averaged over the time-window $[300 - 720]\,\mathsf{s}$, using all the time steps of the simulation to maximize the statistical set. The initial averaging time has been selected some tens of seconds after the plume reached the top. Then, we used the spatial averaging procedure described in Sect. 3.4, in order to allow comparison with integral models and discuss the effect of numerical resolution, LES model and kinematic gas–particle non-equilibrium.

The analysis of the influence of the averaging time-window (see, e.g. Esposti Ongaro and Cerminara, 2016, current issue) has shown that the averaging window size is much more important than the initial averaging time t_0, because long period fluctuations must be smoothed out. Therefore, we have taken the time window as large as possible, even though a time-window $[600 - 660]$ s was recommended and used in the inter-comparison study. On the other hand, $t_0 = 300$ s is enough for the WP to reach its maximum height. The updraft is stationary beyond this time, even though the umbrella is not fully developed. However, this aspect of the analysis deserves more attention for the future.

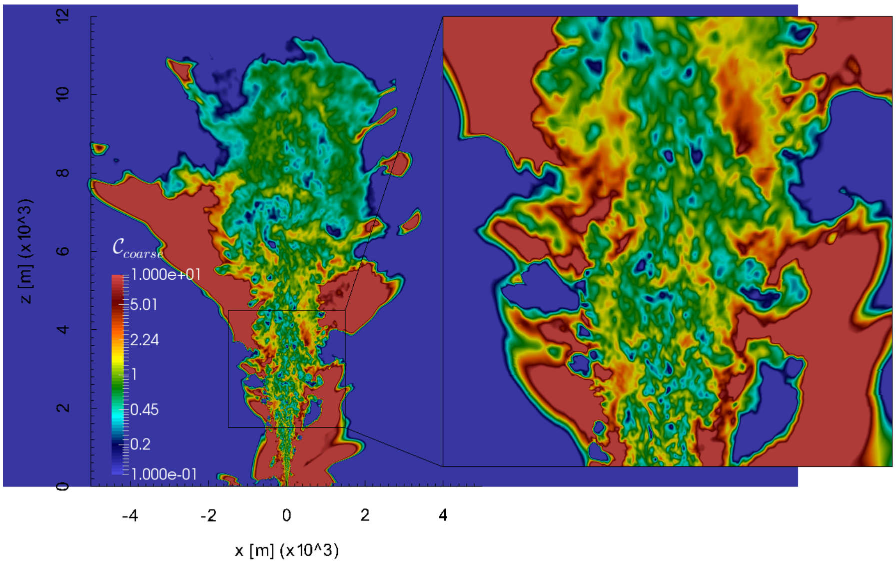

(a) Coarse particles: preferential concentration $\mathcal{C}_{\mathrm{coarse}}$

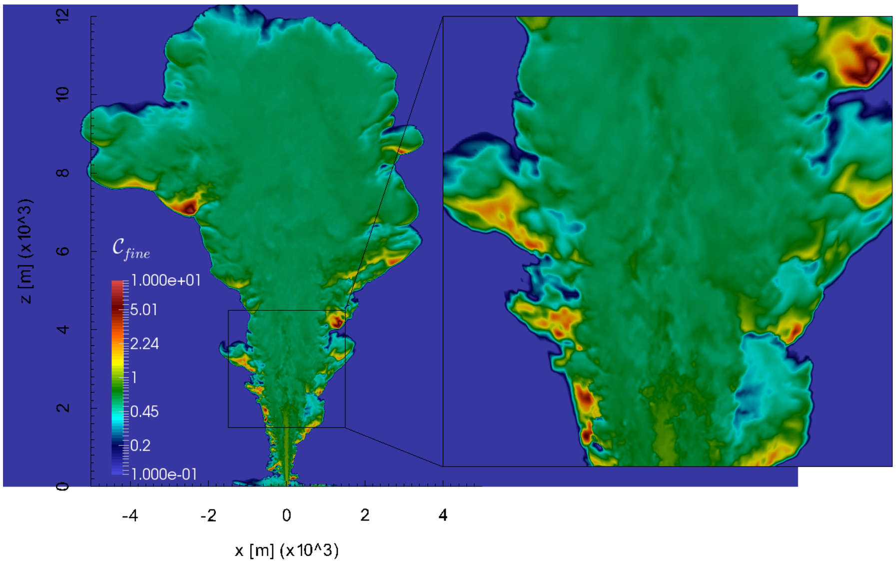

(b) Fine particles: preferential concentration $\mathcal{C}_{\mathrm{fine}}$

Figure 3: Distribution of $\mathcal{C}_{\mathrm{coarse}}$ (a), and $\mathcal{C}_{\mathrm{fine}}$ (b), for the coarser and finer particles across a vertical section at $t = 400\,\mathsf{s}$ (cf. Eq. 20).

Effects of numerical grid resolution. In Figs. 4, we show a detailed comparison of plume mean properties at different grid resolution, by reporting the evolution along the plume axis. In particular we present: (a) the mass flow rate $\pi Q(z)$, (b) the momentum flow rate $\pi M(z)$, (c) the enthalpy flow rate $\pi F(z)$, (d) the solid phase mass fraction $(Y_{\mathrm{coarse}} + Y_{\mathrm{fine}})(z)$, (e) the ratio of coarse on fine mass fractions $(Y_{\mathrm{coarse}}/Y_{\mathrm{fine}})(z)$, (f) the entrainment coefficient $\varkappa(z)$, (g) the plume vertical velocity $U(z)$, (h) the plume radius $b(z)$, (i) the plume–atmosphere density difference $(\beta - \alpha)(z)$, and (j) the plume–atmosphere temperature difference $(T_\beta - T_\alpha)(z)$.

In these panels we first show the development of the fluxes driving the averaged plume properties (mass, momentum, enthalpy). Then, on the basis of these profiles, we use the inversion Eqs. (18) and (19) to recover the mean physical parameters (ash mass fractions, entrainment, velocity, plume radius, density and temperature). The figures show the variability of each mean variable due to the resolution (the high-res, mid-res and low-res simulations are presented) and to the kinematic decoupling model (the [eqEu] model against the [dusty] model). All simulations adopt the [dynWale] SGS model.

Results demonstrate that the numerical model is quite robust and accurate so that even low-resolution simulations are able to capture the main features of the volcanic plume development. However, H_{top} systematically decreases from 12.1 km (a), to 11.3 km (b) to 11.0 km (c) when we decrease the resolution. Analogously, the Neutral Buoyancy Level (NBL) decreases from 7.8 km (a) to 7.2 km (b) to 7.1 km (c). Although the lowest resolution run underestimates the maximum plume height and radius by about 10%, the transition to a super-buoyancy region at about 2000 m above the vent (Woods, 2010) is consistent in the three runs.

In Fig. 4a-c we notice that the effect of mesh resolution has a significant influence on the development of cross-sectional profile of the flux of mass, momentum and enthalpy. Systematically, the more the resolution increases, the more the fluxes increase. However, these differences are mitigated when looking at the physical variables (see Figs. 4d-j). Indeed changing the resolution, the profiles for the variables reported in Figs. 4d-j remain very similar in the plume region, below the umbrella development.

The computed entrainment coefficient is shown in Fig. 4f. Looking at the profiles globally, we notice that it is relatively independent of the grid resolution. For all the runs, a mean value of about $\varkappa \simeq 0.1$ is obtained in the buoyant plume region between 2 and 6 km above the vent. The entrainment coefficient assumes smaller values in the jet region $\varkappa \simeq 0.05 \div 0.07$, coherently with experimental results (Zhou et al., 2001). Interestingly, we find that in 3D simulations the entrainment decreases near the NBL and it becomes negative above that level. This happens because the mass exits from the plume region moving to the umbrella cloud. In this way, the mass flow q of the plume decreases above the NBL and a stationary solution can be achieved. This is not the case in integral plume models with positive entrainment coefficient, where the maximum plume height is reached as a singularity point with divergent mass flow and plume radius (see Figs. C.17a and C.17c in Appendix C).

We conclude that – with the mesh geometry used – mean physical parameters are captured by all the resolutions used, within a 10% error.

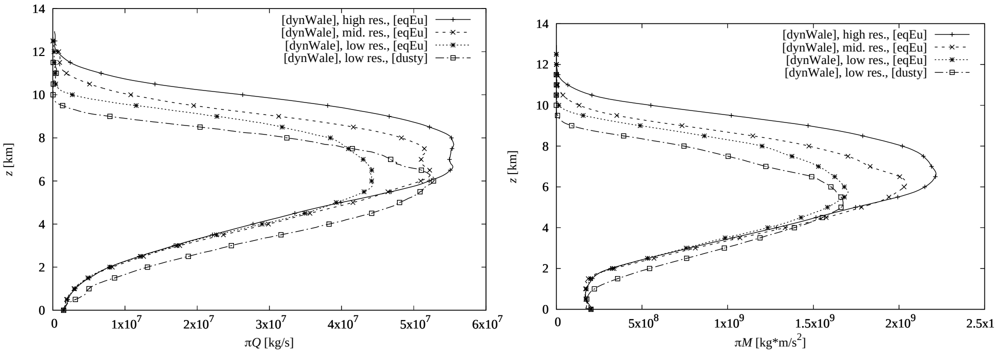

(a) Mass flow rate (b) Momentum flow rate

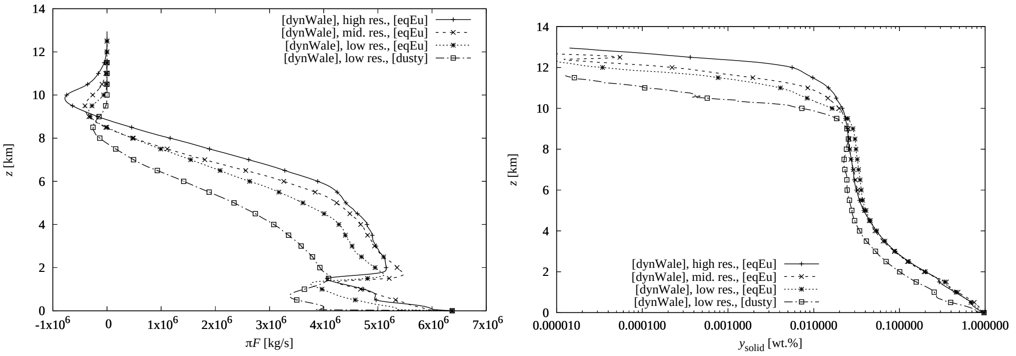

(c) Enthalpy flow rate (d) Solid phase mass fraction

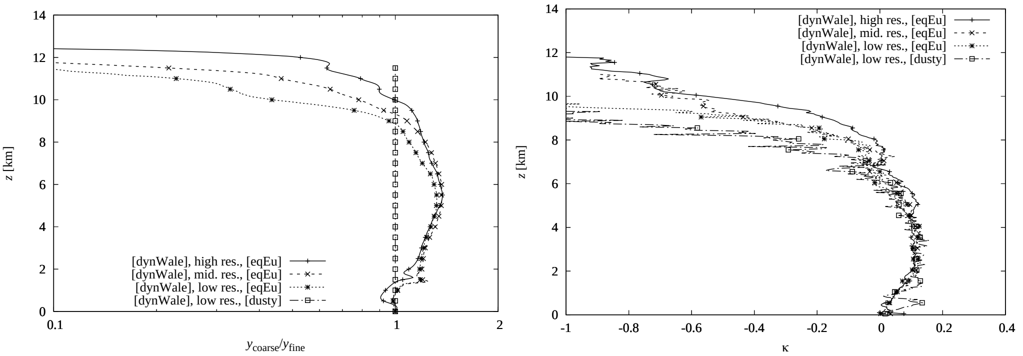

(e) Ratio of coarse on fine mass fractions (f) Entrainment coefficient

Figure 4: (first part) Profiles of the integral variables of WP. Here we compare them by changing the resolution from $\delta = D/32$ (high-res) to $\delta = D/16$ (mid-res) and $\delta = D/8$ (low-res). In the low-res case, we present also the results obtained with the [dusty] model. All runs adopt the [dynWale] SGS model.

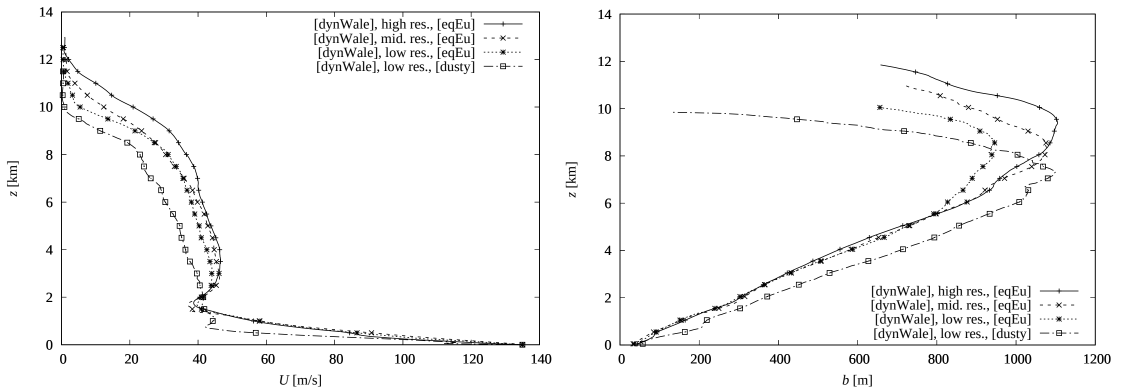

(g) Plume vertical velocity

(h) Plume radius

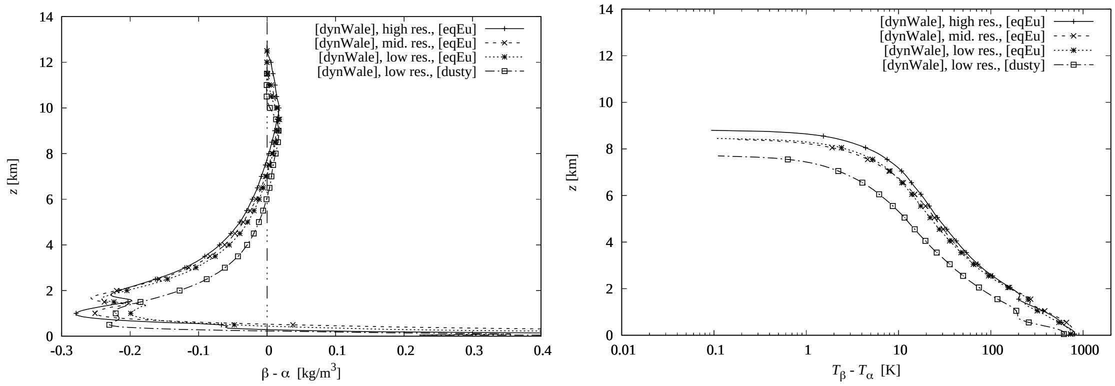

(i) Density difference

(j) Temperature difference

Figure 4: (second part).

Effect of kinematic decoupling: ash jet dragging. The plume mean profiles are influenced by the kinematic gas–particle decoupling in the jet region. Indeed, in Figs. 4, the [dusty] model shows a significantly different behavior with respect to [eqEu] (at constant resolution), with a larger plume radius, a higher entrainment coefficient in the jet region and a less marked jet-plume transition with no further acceleration (without a transition to super buoyancy). The plume height is slightly lower than the non-equilibrium case at the same resolution having $H_{\mathrm{top}} = 9.9\,\mathsf{km}$ and $H_{\mathrm{nbl}} = 6.1\,\mathsf{km}$, respectively. Numerical simulations thus suggest that the effects of non-equilibrium gas–particle processes (preferential concentration and settling) on air entrainment and mixing are non-negligible. These effects are certainly overlooked in the volcanological literature and will be studied more thoroughly in future studies, by applying the present model to other realistic volcanological case studies. However, in the following we present some first results obtained from the simulations so far carried out.

In Figs. 4d-j, we notice that differences between profiles are influenced more by the decoupling between the gas and particles than by the grid resolution. By comparing the low resolution simulations executed with model [eqEu] and model [dusty], we notice that the former tends to shift all plume properties upward. In particular at a fixed height z, the mass and enthalpy fluxes are higher with [eqEu] model, while the momentum flow is slightly lower. These facts are reflected in a higher velocity, temperature and ash mass fractions at a fixed height. On the contrary, the plume radius and the plume entrainment are reduced by the gas–particle decoupling. The motivation for this behavior is found in the differences between [eqEu] and [dusty] models, i.e in the role of particle kinematic decoupling. Particle decoupling acts on the plume dynamics by two main processes: particle settling and turbulent preferential concentration. The former effect would induce the mass fraction of the coarsest ash phase to decrease with height, while the latter induces particles to accumulate in the direction opposite to gas acceleration (cf. Eq. (B.1)). Thus in the jet region, where a strong deceleration is present, decoupling allows the coarse particles to travel more upwards than expected by the dusty gas model. Two-way coupling induces all phases, both the fine particles and the gas, to partially follow the coarse phase. The combined effect of gas–particle kinematic decoupling and the two-way coupling can be seen in particular in Figs. 4g, 4h, 4i, 4j, 4d, and 4e. We refer to this effect as ash *jet dragging.* In Fig. 4j we can see that also the temperature increases because of jet dragging and the plume radius is reduced because the plume is somehow “stretched” by the same effect. It should be noted, however, that herein we have not considered underexpanded plumes, which could generate more complex flow patterns in the jet region (Esposti Ongaro et al., 2008; Carcano et al., 2014). In this case, in fact we could observe first a gas expansion and acceleration followed by an abrupt deceleration due to the formation of the Mach disk.

Plume entrainment. In Fig. 5, we show the development of the entrainment coefficient below the umbrella region. To discuss the differences between simulations, keeping the plot clear, we report the entrainment obtained with the high-res simulation and the key fitting parameters of all the other simulations in legend (the complete entrainment evolution for all the simulations can be found in Fig. 4f).

In the plume region (between about five times the Morton et al. (1956) length scale and the NBL) the simulated entrainment coefficient remains nearly constant. Moreover, it is weakly influenced by the mesh resolution and by the multiphase flow model. In particular, we obtain an entrainment coefficient equal to $\varkappa = 0.103 \pm 0.001$ in the high resolution case. The middle resolution simulation gives an entrainment coefficient which is in the error band of the high-res simulation: $\varkappa = 0.101 \pm 0.002$. Thus, the middle resolution LES is enough refined to capture the correct entrainment coefficient and its error bar. On the other hand the low resolution simulation gives an entrainment coefficient which is underestimated by about 10%. The comparison of the multiphase models [eqEu] and [dusty] does not present significant differences, because the error bars of the two results are overlapping. Moreover, it is worth noting that the standard deviation between the constant fit and the simulated data is decreasing as the resolution increases. This justifies the use of a constant entrainment coefficient by integral one dimensional models in the plume region, from about five times the Morton length scale to the NBL.

In the jet region, the entrainment is not significantly influenced by the resolution, while it is strongly influenced by the multiphase model (see the jet region in Fig. 4f). Thus, the ash jet dragging is influencing the entrainment

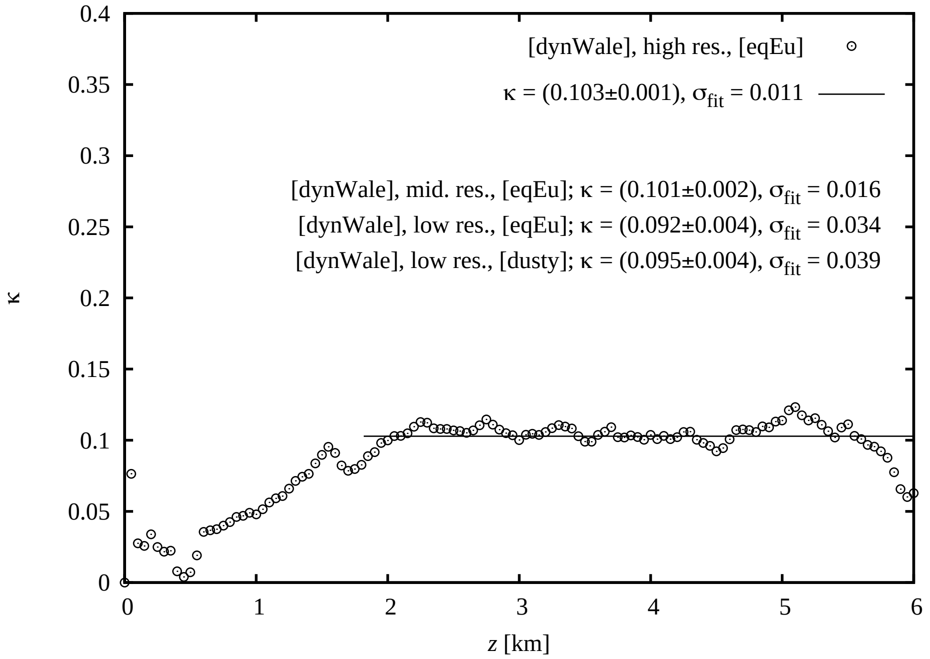

Figure 5: Entrainment coefficient $\varkappa$ of the WP case in the plume region $2 \div 6\,\mathsf{km}$ above the inlet. This is a zoom of Fig. 4f. We show the fit graph obtained at high-res, and the fit results for the other simulations performed.

coefficient, decreasing significantly its mean value and its fluctuations in the jet region below 2 km: [dusty] $\varkappa_{\text{jet}} = 0.0854115 \pm 0.006456$, $\sigma_{\text{fit}} = 0.0413412$; [eqEu] $\varkappa_{\text{jet}} = 0.0557168 \pm 0.004812$, $\sigma_{\text{fit}} = 0.030815$.

4.3. Comparison with integral models

Results shown in Figs. 4 can be compared with those in Fig. C.17, obtained from integral models presented in Appendix C. There, we introduce the integral model ASH1D and its analytical approximation ASH0D. Here are a few differences between the outcomes:

- Plume height. Integral models underestimate the plume height with respect to 3D ones: ASH1D gives $H_{\text{top}} \simeq 9.1\,\mathsf{km}$, while ASH0D gives $H_{\text{top}} \simeq 9.3\,\mathsf{km}$. The 3D simulation with the [dusty] model gives $H_{\text{top}} \simeq 9.9\,\mathsf{km}$.
- Neutral buoyancy level. ASH1D gives $H_{\text{nbl}} \simeq 6.7\,\mathsf{km}$, while ASH0D $H_{\text{nbl}} \simeq 7.1\,\mathsf{km}$. The 3D simulation gives $H_{\text{nbl}} \simeq 6.1\,\mathsf{km}$. Integral models overestimate the plume NBL with respect to 3D ones.
- Plume velocity. The plume velocity at the transition to the super-buoyant regime is higher in the integral models ($\simeq 65\,\mathsf{m/s}$) than in 3D ones ($45\,\mathsf{m/s}$).
- Plume radius. Results from integral models are comparable with those obtained from 3D simulations below the NBL. Above, the behavior is the opposite because of the known limitation of 1D models in describing the umbrella region. While in the former case the plume radius increases, in the latter one it decreases going to zero.

- Plume density, temperature and mass fractions. Integral models predict a slightly faster dilution with respect to the 3D one, in particular in the jet region.

The source of discrepancy between the two groups of models appears to be the entrainment assumption, which works reasonably well in the central plume region, while it is less appropriate in the jet region and above the NBL. In the jet part of the evolution, the Ricou and Spalding (1961) model is overestimating the quantity of atmospheric air entrained. This is due to the weakness of both the entrainment model and the self-similarity hypothesis near the vent. Thus, the integral plume model is diluting faster than in 3D simulations, mixing is more efficient, buoyancy is stronger and the plume goes higher, reaching a NBL 10% higher than that provided by 3D simulations. Above the NBL, assuming a constant entrainment coefficient leads to a wrong behavior, where the plume radius diverges instead of going to zero. This discrepancy adds another source of error to the description of the plume profiles since it generates a significant underestimation of the column height. In 3D simulations the entrainment becomes negative above the NBL, because the plume loses mass, which moves to the umbrella. The momentum decrease is thus slower than in the integral model.

Plume conserved quantities. 1D integral plume models predict that there are two integral quantities that are approximatively conserved along the plume height (Cerminara, 2015): $\mathcal{U}_{\mathrm{RS}}$ (C.7) and $\mathcal{U}_m$ (C.8). There, q, m and f are defined as the non-dimensional fluxes corresponding to their dimensional counterpart (in capital letter), while the coefficient γ_{c} is a non-dimensional parameter measuring the stability of the volcanic column (see Appendix C.2). These two integral of motion can be evaluated using 3D results. The comparison between the expected constant profile of $\mathcal{U}_{\mathrm{RS}}$ and $\mathcal{U}_m$ and the profile computed by the 3D model allows to get more insight into the goodness of 1D model approximations.

$\mathcal{U}_{\mathrm{RS}}$ depends linearly on $l_{\mathrm{c}}(q) \simeq q^2$ (see Eq. (C.9)) and $m^{\frac{5}{2}}$, while $\mathcal{U}_m$ depends linearly on $(f-\gamma_{\mathrm{c}})^2$ and m^2. Where a linear relationship between these terms is found, this means that the first integral of motion can be considered as a constant and the 1D approximation is applicable. In Fig. 6, we show the behavior of these quantities in the 3D simulations.

The linear behavior predicted by the 1D model is obtained, provided that some of the parameters of the integral model are modified. In particular, when testing the conservation of first integral $\mathcal{U}_{\mathrm{RS}}$, the parameter a_q (see Appendix C.2) has to be increased significantly (see Fig. 6). In this way, $\mathcal{U}_{\mathrm{RS}}$ remains nearly constant from the vent elevation to the NBL (where m reaches its maximum). On the other hand, $\mathcal{U}_{\mathrm{RS}}$ is not conserved above the NBL. This is in agreement with the entrainment profile, which is not constant above the NBL.

The other conserved quantity $\mathcal{U}_m$ is instead defined independently from the entrainment assumption. In the 3D results, in order to have $\mathcal{U}_m$ approximately constant along the plume, we increased slightly γ_{c} (see Fig. 6). Then, $\mathcal{U}_m$ can be considered approximately constant all through the plume height, even during the buoyancy transition at the NBL. This result is in agreement with the independence of $\mathcal{U}_m$ from the entrainment assumption. However, in the region near the vent $\mathcal{U}_m$ is subject to a sudden change that we identify in Fig. 6 with $\Delta\mathcal{U}_m \simeq -0.373$. This behavior cannot be attributed to the non-Boussinesq

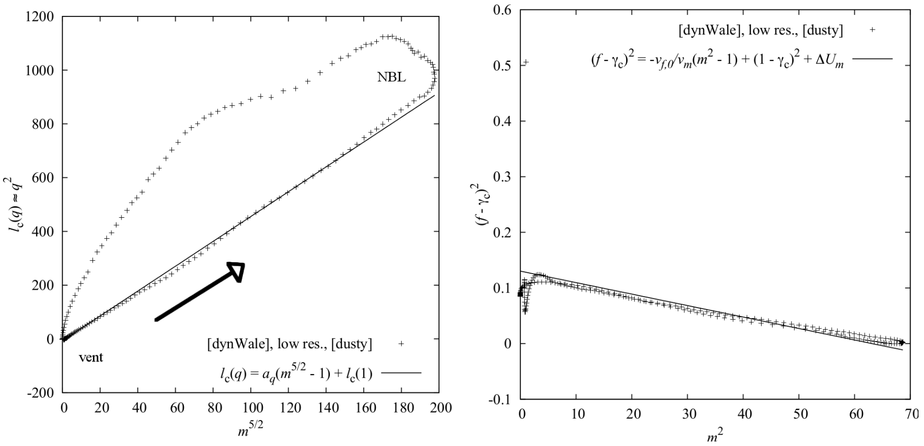

Figure 6: Behavior of conserved quantities of ASH0D as calculated from 3D simulations of the WP scenario. Here we modified some of the plume parameters to obtain a better behavior of the conserved quantities (see discussion): $a_q = 1.65 \rightarrow a_q = 4.62$, $\gamma_c = 0.252 \rightarrow \gamma_c = 0.292$. Moreover, we used the value of $v_{f,0} = 2.66 * 10^{-4}$ obtained averaging the atmospheric profile: $\mathcal{N}_0 \simeq 1.40 * 10^{-2}$ Hz. Each point corresponds to a different height, evolving as indicated by the arrow: from the vent to the maximum height, through the NBL.

regime near the vent, because $\Delta\mathcal{U}_m \simeq 0$ even without this approximation (by using ASH1D). More likely, this behavior is attributed to the shape of the averaged horizontal profiles of the 3D plume. Indeed, the self-similarity hypothesis could not be met near the vent (Esposti Ongaro and Cerminara, 2016; Cerminara, 2016). Further studies and numerical simulations are needed to better understand the presented behavior.

5. Strong plume

The strong plume (SP) case represents a Plinian scenario with mass eruption rate $\pi Q_0 = 1.5{*}10^9$ kg/s. Initial and boundary conditions are reported in Tab. 1. In this section we discuss the results obtained from 3D numerical simulations of the SP. The main physical differences between this plume and the WP are the following: 1) the plume is supersonic at the vent, since the mixture speed of sound is 157 m/s, while the exit mean velocity is 275 m/s; 2) the plume has more water than WP, this reflects in a smaller density contrast; 3) the Richardson number v_m is four times larger, thus the non-dimensional Morton length scale decreases by about a factor of 2; 4) the stratification length scale decreases by about a factor 23, driving the transition between jet and plume at a height comparable with the NBL.

We have performed a number of different simulations, modifying both the resolution and the LES model. In this section, we mainly present the results obtained with the [dynWale] model at the finer resolution $\delta = D/32$. Then we study how the averaged plume properties are influenced by the grid resolution and the LES model. In particular, alongside the high-res simulation, we used a mid-res grid ($\delta = D/16$) and a low-res grid ($\delta = D/8$). Then we compared results obtained with [dynWale] with those obtained with [moin], [oneEqEddy] or without subgrid model [noM]. Finally, we measure the effect of kinematic non-

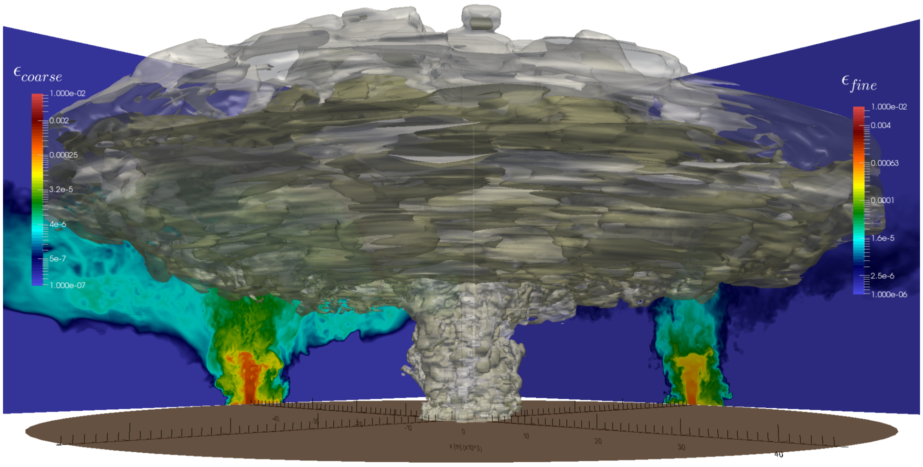

Figure 7: 3D numerical simulation of the SP case, 1000 s after the beginning of the eruption (inlet conditions are in Tab. 1). The two isosurfaces in 3D rendering correspond to the threshold $\epsilon_s = 10^{-7}$ of the fine (light white) and coarse (light sand) ash volume fractions.. The maximum height of the fine class isosurface is approximatively 43 km. The two-dimensional plots represent the distribution of the volume concentration of coarse (left) and fine (right) particles across vertical orthogonal slices crossing the plume axis. See color palette for volume concentration values.

equilibrium, comparing the results obtained with the [eqEu] model with those obtained using [dusty].

As already done for the WP, we *a priori* evaluate the Stokes number associated with this eruption, based on the most energetic turbulent eddy scale $\tau_D \simeq 1.5\,\mathrm{s}$. We obtain $\mathrm{St}_{\mathrm{coarse}} \simeq 0.27$ and $\mathrm{St}_{\mathrm{fine}} \simeq 1.2 * 10^{-3}$. From the a-posteriori analysis based on the Taylor microscale, we find: $\mathrm{St}_{\mathrm{coarse}} \simeq 0.06$ and $\mathrm{St}_{\mathrm{fine}} \simeq 3 * 10^{-4}$, for the finer mesh resolution. Thus, we expect that the kinematic decoupling is less important in the SP than in the WP case, and that the [eqEu] model is well justified even for this simulation.

5.1. Large Eddy Simulations results

The computational grid is extended $66b_0 \times 71b_0$ in the radial and vertical directions, respectively. For the highest resolution run, the cells have a minimum size $\delta = D/32$. As for the WP simulations, there is no radial grading in the plume region, while outside that region a radial grading factor of 1.011 is applied. The mesh opening is $\tan\theta = 0.0846$. Along z, 2112 cells are utilized. The minimum vertical cell size is $\delta = D/32$, and a grading factor of 1.000657 is imposed. The azimuthal resolution is again $\pi/32$, with a total number of cells equal to $8,785,920$.

Numerical simulation of 1000 s of eruption time required: 1.5 h for the low-res case (on one Intel-I7 quad-core processor at 2.8GHz); 39 h for the mid-res case (on 4 AMD 16-core processors at 2.3GHz); 72 h for the high-res case (on 1024 cores of the CINECA IBM BG/Q machine).

Large scale dynamics. Figs. 7 and 8 show the development of the volcanic plume at $t = 1000\,\mathrm{s}$ from the beginning of the simulated event. The plume at the vent

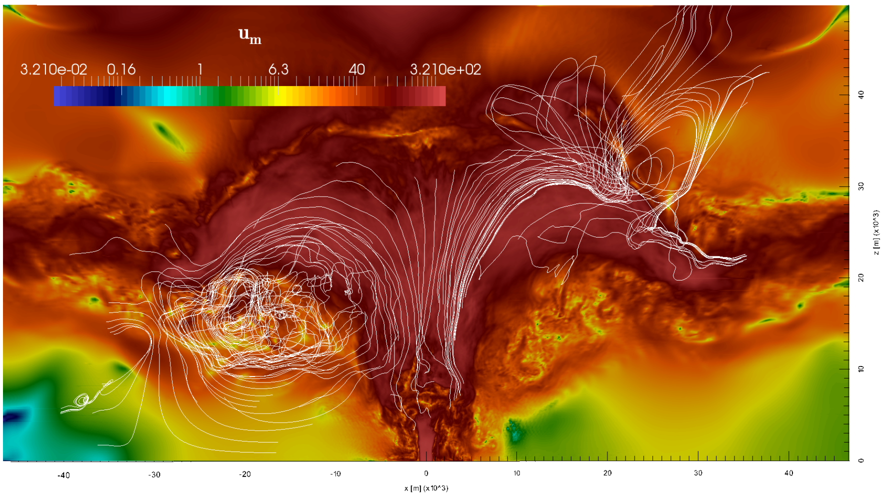

Figure 8: Vertical section of the instantaneous value of the mixture velocity modulus (in logarithmic scale, [m/s]) at $t = 1000\,\mathsf{s}$ from the beginning of the eruption, and corresponding velocity streamlines.

is denser than the surrounding atmosphere, but the initial inertia allows most of the mass to mix with the atmosphere, thus reversing the buoyancy from negative to positive. The transition takes place through the development of a fountain, and a *suspended flow* horizontally spreading over the jet at about 5 km height (Neri and Dobran, 1994; Suzuki and Koyaguchi, 2012). However, in this simulation part of the mass collapses to the ground, forming pyroclastic density currents and a co-ignimbrite plume surrounding the jet core. By inspection of the simulation results, it is computed that approximatively 17% of the mass of the column collapses to the ground and is subsequently re-entrained in the main column through the co-ignimbrite plume. The plume reaches a neutral buoyancy condition at about 18.9 km above the vent. Inertia allows the plume to reach its maximum height at $H_{\mathrm{top}} \simeq 43\,\mathsf{km}$. Then the top of the plume collapses over the NBL, spreading radially to the umbrella cloud. The updraft induces a significant atmospheric perturbation driving the development of the umbrella.

The more evident structure, peculiar of the SP, is the large toroidal eddy under the umbrella cloud. Less apparent, but still very important, is another toroidal eddy developing around the jet, under the suspended flow. These two features are present in the instantaneous fields as pulsating turbulent structures, however they are clearly recognizable also in the time-averaged fields (e.g. Dobran et al., 1993; Cerminara, 2016). Fig. 8 shows the streamlines of the velocity field in a vertical slice of the whole simulated plume. Re-entrainment plays an important role, causing part of the settled and collapsing particles to be re-entrained into the plume, to be transported again upwards (Dobran et al., 1993). Velocity fluctuations are stronger along the plume margins, while the velocity appears to be more stable near the plume axis. The jet region exhibits a complex behavior, being surrounded by a collapsing layer, a re-entrainment region and an ascending co-ignimbrite (Cerminara, 2016). A quantitative dis-

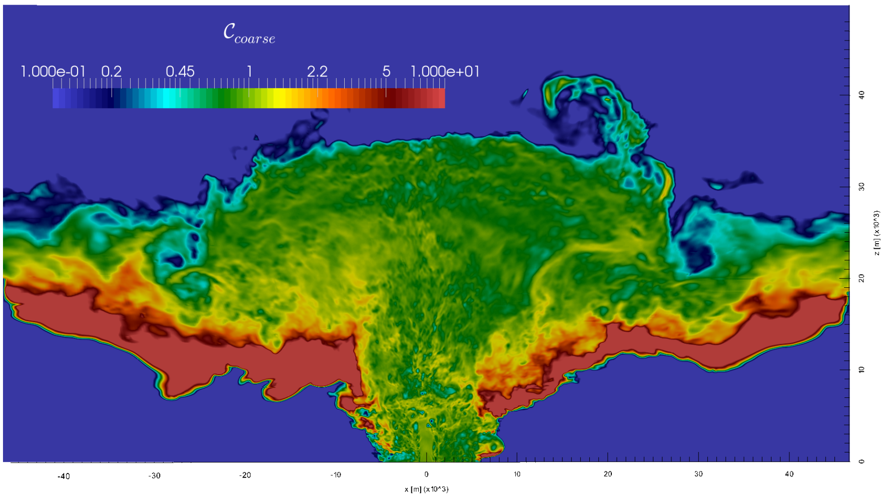

(a) Coarse phase preferential concentration

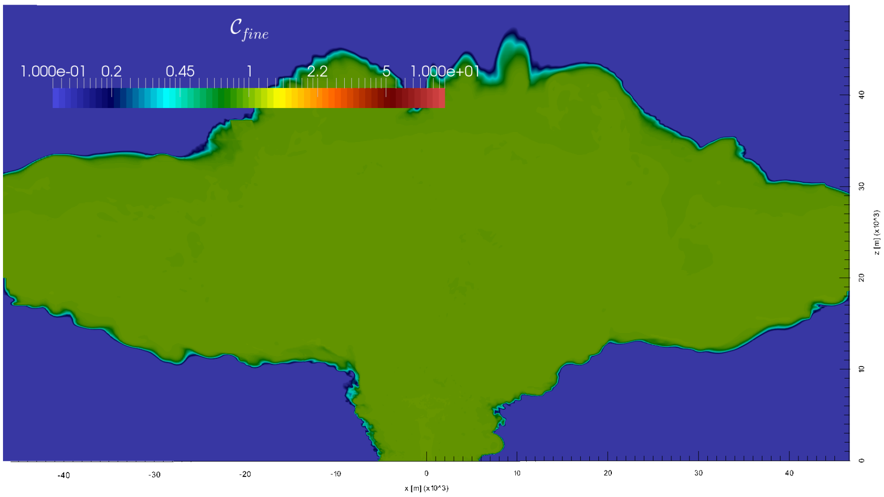

(b) Fine phase preferential concentration

Figure 9: Distribution of $\mathcal{C}_{\text{coarse}}$ (a), and $\mathcal{C}_{\text{fine}}$ (b), for the coarser and finer particles across a vertical section at $t = 1000\,\mathsf{s}$ (cf. Eq. 20).

cussion of the influence of the plume collapse and particle re-entrainment can be found in the next sections, where we study the time-averaged properties of this volcanic plume. However, before discussing that, we focus on two additional aspects of the instantaneous fields: kinematic non-equilibrium and turbulent infrasound generation.

Kinematic non-equilibrium effects. To illustrate the preferential concentration, we use again the quantity $\mathcal{C}$, Eq. (20). In Fig. 9 we show the distribution of preferential concentration in an axial slice of the plume. We notice that the fine ash phase is practically coupled with the mixture velocity field, while the coarse phase is not. As already noticed in the WP case (see Fig. 3a), the top of the plume is depleted of coarse particles which tend to settle down. The area of the plume where particle fallout is stronger is red. Inside the plume, turbulence makes the coarse particles to preferentially concentrate, creating zones with higher ash mass fraction (yellow) and zones with lower mass fraction (cyan and blue). Coarse ash clustering is stronger in the jet-plume transition zone and in the zone below the umbrella cloud. Preferential concentration is weaker for this plume with respect to the WP case, as expected from the analysis of the Stokes number. For this reason, as we discuss below comparing the models [eqEu] and [dusty], ash *jet dragging* is present but weakened in the SP case.

Turbulent infra-sound generation. The plume presented in this section generates large eddies, comparable with the size of the vent ($\simeq 10^3\,\mathsf{m}$). Turbulent eddies generate pressure perturbations because of their centrifugal acceleration (see e.g. Lesieur et al., 2005). In Fig. 10 we show the shape of these perturbations, highlighting that the source of infrasound is not only the vent, but also the large eddies. In this figure, the perturbations are highlighted by showing, in colored logarithmic scale, the magnitude of the acceleration field of the gas phase. The infrasonic signal can be measured from the ground, extracting important information about the plume dynamics (cf. Johnson and Ripepe, 2011). In Matoza et al. (2009) infrasonic spectra from volcanic eruptions have been compared with large-scale and fine-scale similarity spectra as measured by Tam et al. (1996).

In Fig. 11, we show the simulated pressure fluctuation at ground level, 15 km far from the vent center, in the time window $t \in [0, 13]\,\mathsf{min}$. As usually done by real infrasound microphones (Matoza et al., 2009), the pressure signal is convoluted with a kernel window cutting the frequencies smaller than $0.03\,\mathsf{Hz}$, to study only pressure fluctuations and not absolute variations. The resulting spectrum is compared with the similarity spectrum generated by large-scale turbulence measured by Tam et al. (1996). The fit is in satisfactory agreement and comparable with results obtained from direct volcanic observation (see Matoza et al., 2009). We obtained a peak in $E_p(\mathrm{Str}_D)$, for $\mathrm{Str}_D = 0.32 \pm 0.01$, a value comparable with that expected from experimental results (see Lesieur et al., 2005; Cerminara et al., 2016). We show also the slope $\mathrm{Str}^{-11/4}$ measured by Tam et al. (1996) for supersonic jets for $\mathrm{Str} > 2.5\,\mathrm{Str}_D$. It is worth noting that our result could be influenced by the reflective boundary conditions we are using. In future studies we plan to modify the atmospheric boundary conditions in order to make them non-reflective.

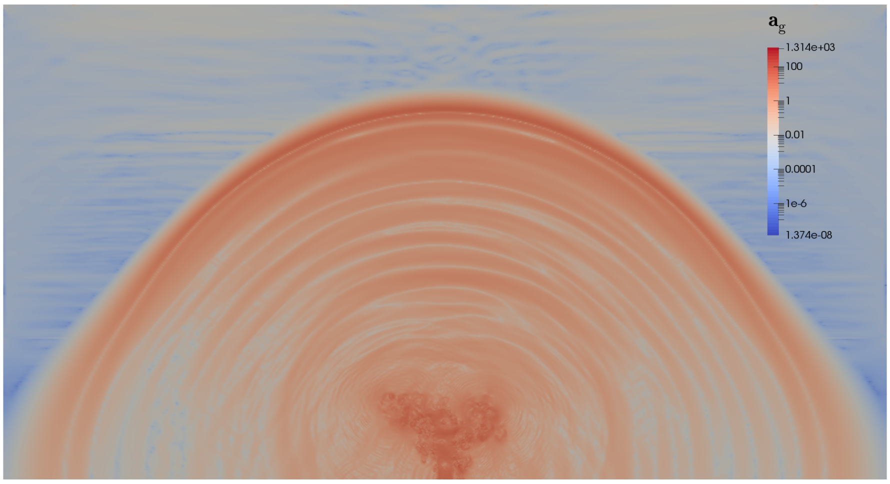

Figure 10: Infrasonic signal generated by the turbulent eddies of the SP. Here the infrasonic perturbation is visualized by using the magnitude of the acceleration field $\boldsymbol{a}_{\mathrm{g}}$, in logarithmic color scale [$\mathsf{m/s^2}$], 120 s after the eruption started.

5.2. Plume mean properties

Similarly to what we have done for WP, we here analyze the profiles of the main averaged plume variables along the vertical extension of the plume. The averaging technique is described in Sect. 3.4. Here we have used an averaging time window $\mathcal{T} = [1000, 2000]\,\mathsf{s}$.

Effect of grid size, LES model and non-equilibrium. While in the first part of this section we have commented results from the high-res [dynWale] simulation, in this sub-section, we present three groups of figures to study quantitatively the effect of the mesh resolution (Fig. 12); the effect of the subgrid scale model (Fig. 13); the effect of the kinematic decoupling model (Fig. 14). Moreover, in Fig. 15 we compare the entrainment coefficient as obtained from all the SP simulations presented.

The effect of the resolution can be investigated by comparing the simulations high, mid, and low resolution performed with [dynWale] (see Fig. 12). The plume heights based on the 1 wt.% of a tracer are respectively: $H_{\mathrm{top}} = 43$, 41, 43 km; the plume NBLs are, respectively, $H_{\mathrm{nbl}} = 18.8$, 18.4, 17.7 km. The relative error due to resolution is less than 6%. Similarly to what we have found for WP, even in the SP case results are quite robust and accurate and even the low resolution simulation is able to capture the main features of the averaged volcanic plume. However, the resolution has a stronger effect on this eruption than on WP.

In Figs. 12g and 12j, we notice that the velocity is underestimated and the temperature is slightly overestimated by the low-res simulation. These are the most evident differences due to grid resolution, caused by an underestimation of the momentum and enthalpy fluxes (see Fig 12). We conclude that a simulation with a finer resolution is desirable to stabilize the plume averaged results.

Moving to the effect of the subgrid scale model, we have two groups of simulations to be compared in Fig. 13. The first group analyzes [dynWale] and [noM], both at high resolution. In this way we can estimate the net effect of the

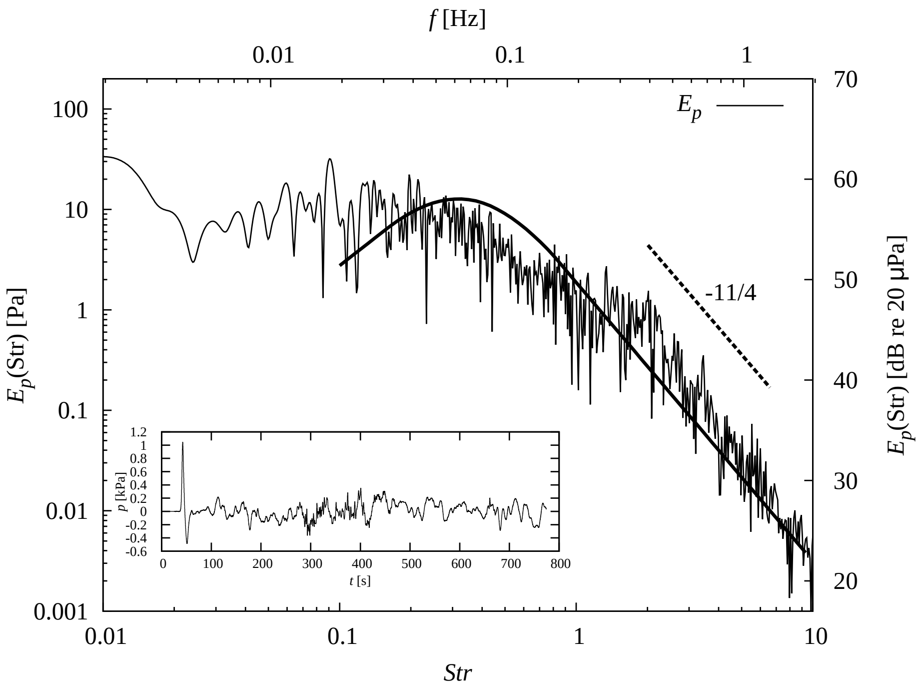

Figure 11: Infrasonic spectrum of the pressure fluctuations as measured from a probe placed at the ground level 15 km from the vent center, in the time window $t \in [0, 13]$ min. The frequency is expressed both in its dimensional (f) and non-dimensional (Str $= f\,D/U_0$) formulation. Pressure fluctuations E_p are represented both in logarithmic scale and in dB scale relative to 20 μPa. The slope $\mathrm{Str}^{-11/4}$ is shown in bold dashed line. The experimental large-scale similarity spectrum is presented in bold solid line (see Tam et al., 1996). The inset shows the pressure fluctuation signal in kPa until $t \simeq 13$ min.

LES model. The height of the plume is, respectively, equal to $H_{\mathrm{top}} \simeq 43$ and 40 km; while the NBL is $H_{\mathrm{nbl}} \simeq 18.8$ and 18.2 km, respectively. Thus, the subgrid model tends to increase the plume height and the plume NBL with a relative discrepancy of the order of 7% and 3%, respectively. The entrainment coefficient without subgrid model ([noM]) does not significantly change in average although its fluctuations increase ($\sigma_{\mathrm{fit}} \simeq 0.20$ vs 0.14 in the legend of Fig. 15). The main differences in the plume profiles are caused by the underestimation of the mass and enthalpy fluxes by [noM] above the jet-plume transition, inducing the slight underestimation of the plume radius, density, temperature, and solid phase mass fractions. Using a subgrid model improves the quality of the averaged results: the mid-res simulations with subgrid model are closer to the high-res simulation than the high-res with [noM].

The second group of profiles presented in Fig. 13 compares [dynWale], [moin], and [dynOneEqEddy] at middle resolution. As pointed out above, the entrainment coefficient agrees among all the simulations and, this time, also fluctuations are comparable. In particular, $\varkappa$ is underestimated by [dynWale], comparable with the high-res simulation for [moin] model, and is overestimated by [dynOneEqEddy]. These small differences are reflected in the averaged plume profiles, making the mid-res simulation performed with [moin] the most accurate one. However, we can conclude that the effect of the subgrid model used is weaker than the effect of the resolution, in the range of variation investigated.

The last group of profiles is shown in Fig. 14. In this figure we illustrate the effects of the kinematic decoupling between the ash particles and the gas phase. In this case, the decoupling is much weaker than in the WP one. Indeed, as pointed out above, the Stokes number of these particles can be estimated, on average, as $\mathrm{St}_{\mathrm{coarse}} \simeq 0.06$, against $\mathrm{St}_{\mathsf{coarse}} \simeq 0.1$ we have found for the 1 mm particles in WP. This apparent slight difference induces a significant effect on the averaged plume properties. The ash jet dragging effect is now much weaker and can be seen clearly only on the enthalpy flux profile Fig. 14c and more weakly in the mass flux profile Fig. 14a. This is reflected with more evidence in the plume radius, velocity and mass fraction ratio profiles (Figs. 14h, 14g and 14e). As in the WP case, the plume radius is initially reduced by the jet dragging inducing a larger plume radius above the NBL. The velocity increases under the NBL due to kinematic decoupling, while above that level, velocity is larger in the dusty-gas simulation. The plume height and NBL increase because of kinematic decoupling: they move from $H_{\mathrm{top}} \simeq 39\,\mathsf{km}$ and $H_{\mathrm{nbl}} \simeq 18.2\,\mathsf{km}$ with the [dusty] model to $H_{\mathrm{top}} \simeq 41\,\mathsf{km}$ and $H_{\mathrm{nbl}} \simeq 18.5\,\mathsf{km}$ with the [eqEu] model.

Entrainment coefficient. In Fig. 15, we report the entrainment coefficient obtained for all the simulations presented in this Section. We fit the entrainment coefficient computed by using Eq. (19) with a constant value from the vent to approximately the NBL: $H_{\mathrm{nbl}} = 16\,\mathsf{km}$. Surprisingly, we obtained quite stable results, even at different resolution, subgrid model and kinematic decoupling model: $\varkappa = 0.24 \pm 0.02$. However, we notice that the fluctuations of the entrainment coefficient σ_{fit} are significantly larger than in the WP case. Even if the entrainment coefficient oscillates around a constant value, the standard deviation in this plume is significantly higher: $\sigma_{\mathrm{fit}} \simeq 0.14$ for the reference high resolution simulation.

It is worth noting that the entrainment coefficient shown in Figs. 15 and 5 has been evaluated by using Eq. (19), thus without adding in Eq. (C.1a) either a sink term due to particle fallout, a source term due to particle re-entrainment, or a correction keeping into account partial plume collapse. Consequently, the resulting entrainment coefficient contains all these effects, because they are present in our 3D simulations. This could be an explanation of the larger value of the σ_{fit} of the entrainment coefficient computed for the SP with respect to the WP case. A larger value of the σ_{fit} is due to the strong oscillations of the entrainment $\varkappa$ around the fitted value, which makes the self-similarity assumption not valid for this case. Indeed, as it can be noticed from Figs. 7, 8 and 9, the entrainment around the plume edges is not as well organized as for the WP case. In this case, the plume edge is bounded by complex structures which seem to be quite important from qualitative analysis of the figures mentioned above. Other sources of variation appear to be the large eddies underneath the umbrella cloud, which certainly influence the rate of entrainment of the plume below the NBL. Moreover, the plume partially collapses in the jet region, causing the entrainment coefficient to decrease and eventually to go below zero. This fact can be seen in Fig. 15, above the jet-plume transition at $z \simeq 5$ km. Above that height the entrainment coefficient presents two minima, corresponding to the heights where SP loses more mass.

Despite this variability, the results of the fit from the high-res and the mid-res

Mesh resolution

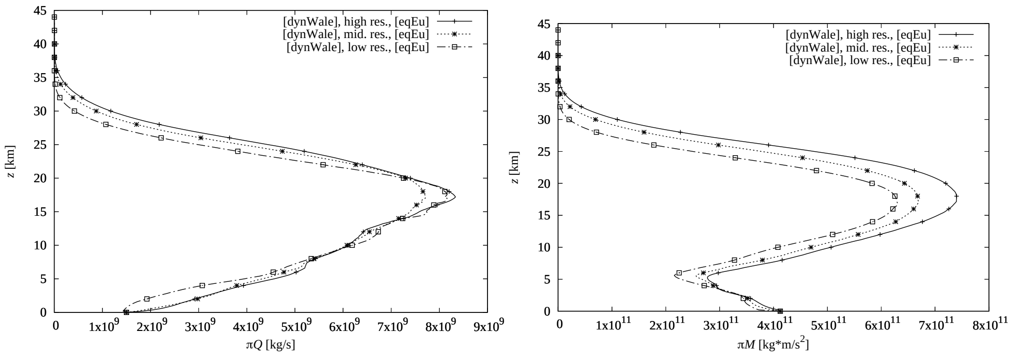

(a) Mass flow rate

(b) Momentum flow rate

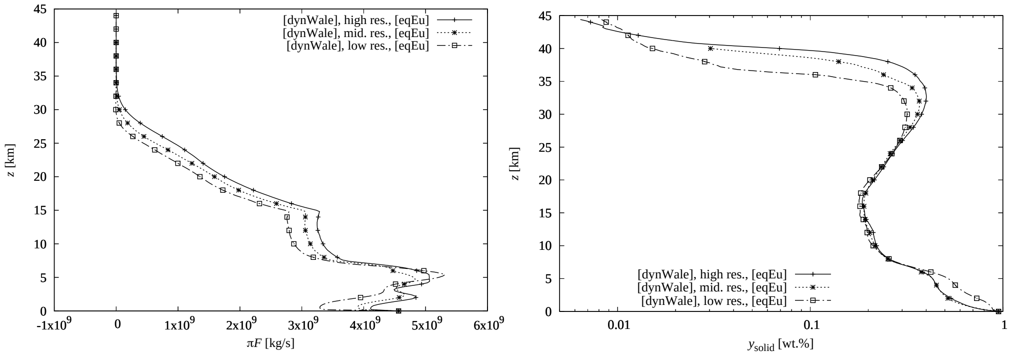

(c) Enthalpy flow rate

(d) Solid mass fraction

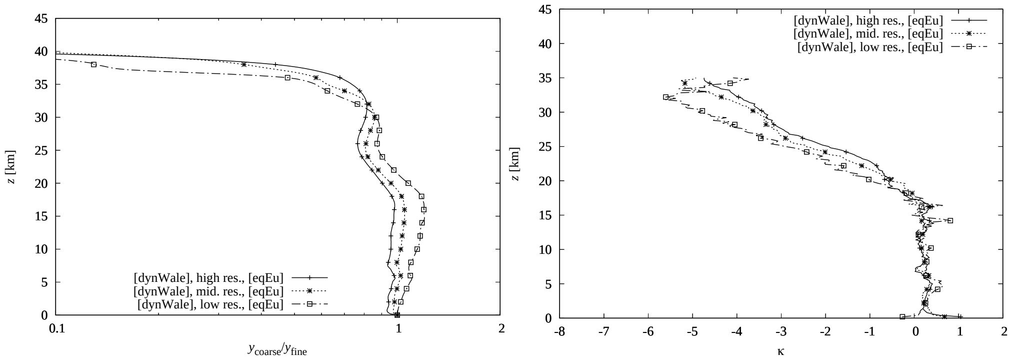

(e) Ratio of coarse on fine mass fractions

(f) Entrainment coefficient

Figure 12: (First part) Influence of the mesh resolution on the profiles of the integral variables of SP. Here we compare them by changing the resolution from $\delta = D/32$ (high-res) to $\delta = D/16$ (mid-res) and $\delta = D/8$ (low-res). All runs adopt the [dynWale] model.

Mesh resolution

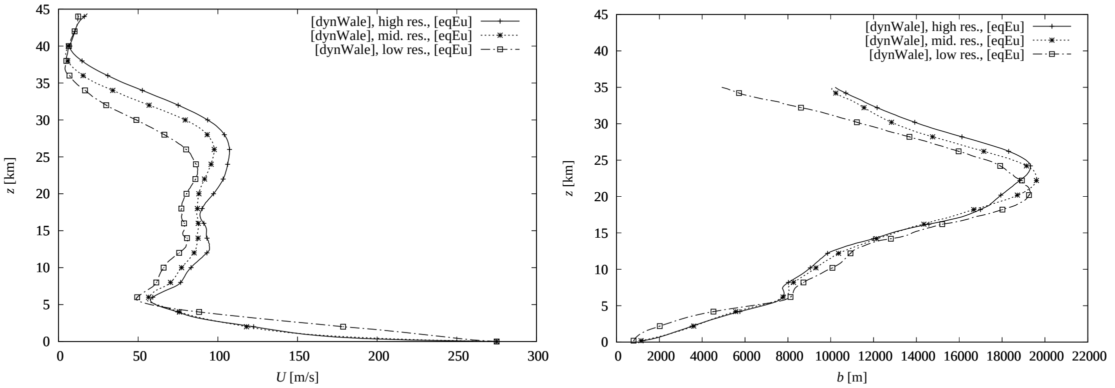

(g) Plume vertical velocity

(h) Plume radius

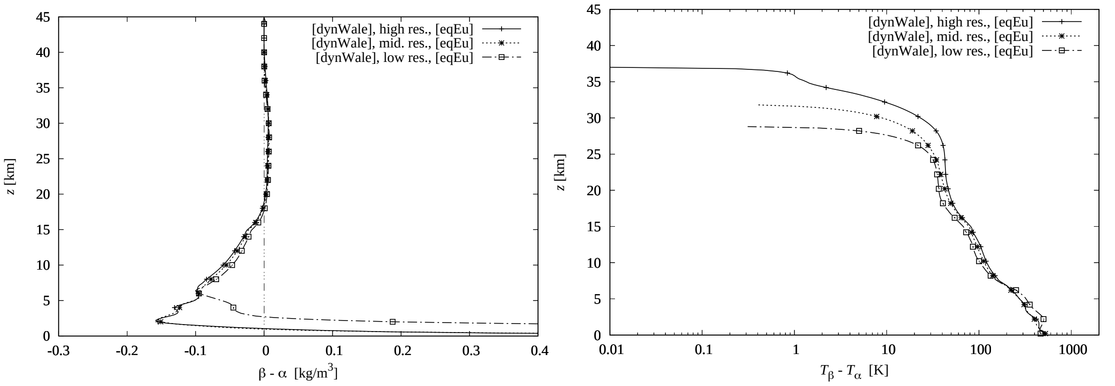

(i) Density difference

(j) Temperature difference

Figure 12: (Second part).

simulations are in agreement, with their respective error bars overlapping. The low resolution simulation is overestimating the entrainment coefficient, modifying the plume properties as commented above. However, all the other simulations at high- and mid-resolution give an entrainment coefficient in agreement with the reference simulation. The kinematic decoupling induces a negligible increase of the entrainment coefficient below the NBL: from $\varkappa = 0.23 \pm 0.01$ in the [dusty] case, to $\varkappa = 0.24 \pm 0.01$ in the [eqEu] one.

5.3. Comparison with the dusty-gas model

As we have done for the WP eruption, in this section we compare results obtained from 3D simulations of the SP eruption with those presented in Sect. Appendix C. Here are a few differences between the outcomes showed in Fig. C.18:

- Plume height. Integral models described in Sect. Appendix C capture the plume height. The ASH1D model (C.1) gives $H_{\mathrm{top}} \simeq 39\,\mathsf{km}$, as the 3D simulations with the [dusty] model. The ASH0D (see Sect. Appendix C.2) overestimates it, with $H_{\mathrm{top}} \simeq 43.5\,\mathsf{km}$.

LES subgrid model

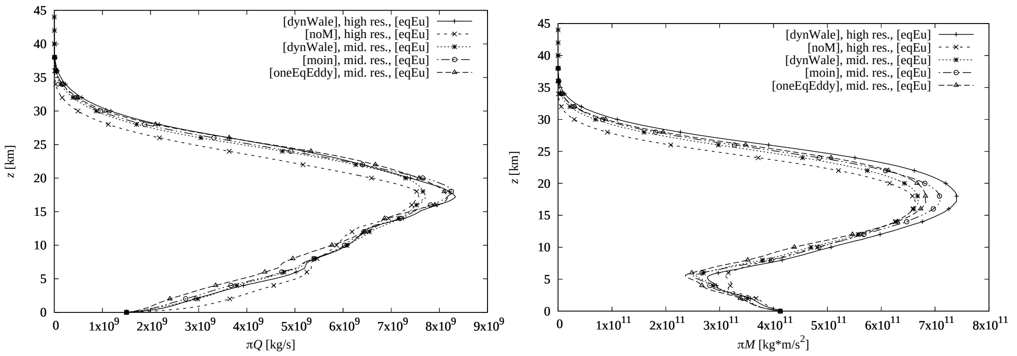

(a) Mass flow rate

(b) Momentum flow rate

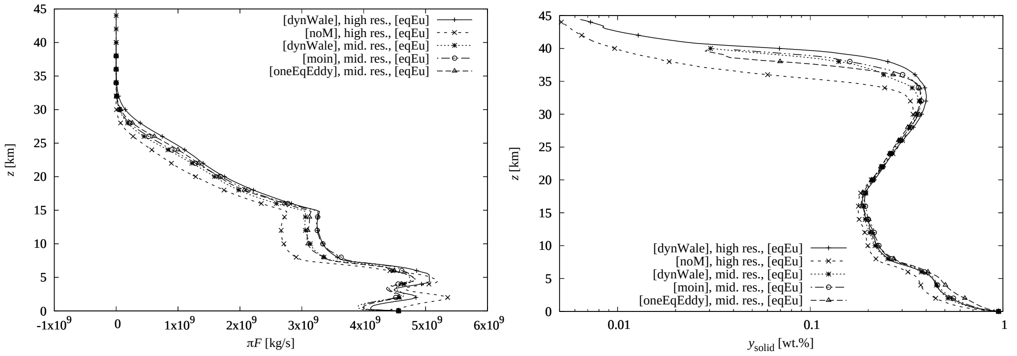

(c) Enthalpy flow rate

(d) Solid mass fraction

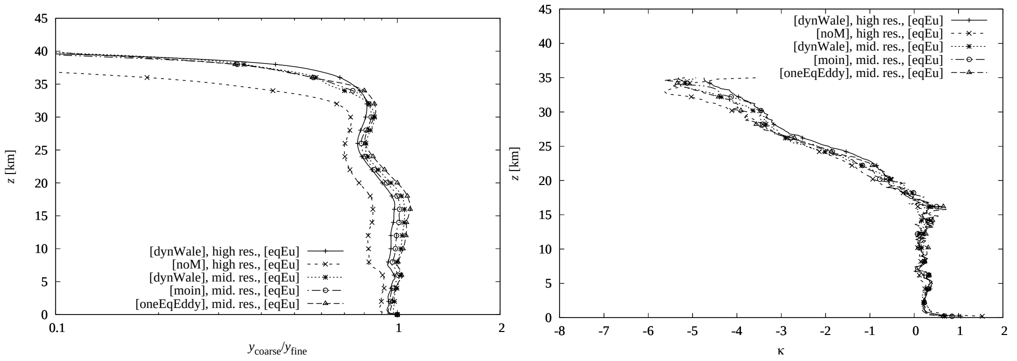

(e) Ratio of coarse on fine mass fractions

(f) Entrainment coefficient

Figure 13: (First part) Influence of the subgrid LES model on the profiles of the integral variables of SP. Here we compare them by using high and middle resolutions. In the high resolution case, we present the results obtained without subgrid model [noM], while in the middle resolution case [moin] and [oneEqEddy] are shown.

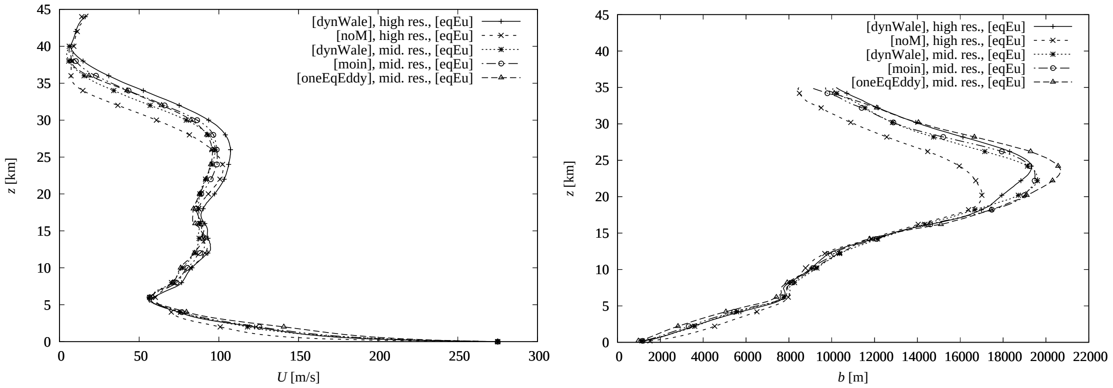

(g) Plume vertical velocity

(h) Plume radius

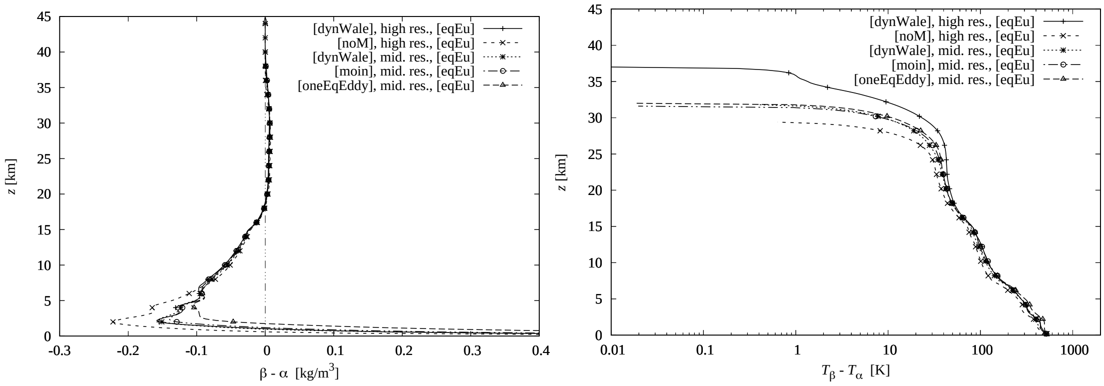

(i) Density difference

(j) Temperature difference

Figure 13: (Second part).

- Neutral buoyancy level. ASH1D gives $H_{\rm nbl} \simeq 24.9\,\mathsf{km}$, while ASH0D $H_{\rm nbl} \simeq 32.5\,\mathsf{km}$. 3D simulation gives $H_{\rm nbl} \simeq 18.2\,\mathsf{km}$. Integral models overestimate the plume NBL.

- Plume velocity. The plume velocity provided by the integral models is significantly higher than that provided by the 3D simulation. While in the former case the velocity in the jet-plume transition height is around $160\,\mathsf{m/s}$, in the 3D simulation it is about $50\,\mathsf{m/s}$.

- Plume radius. The plume radius is strongly underestimated by integral models. The radius in the jet-plume transition is $\simeq 3\,\mathsf{km}$ against $\simeq 5.5\,\mathsf{km}$ in 3D simulations, while close to the NBL ($z \simeq 20\,\mathsf{km}$) it is $\simeq 10\,\mathsf{km}$ against $\simeq 17.5\,\mathsf{km}$ in the 3D simulation. Above that height the behavior is the opposite. While in the former case the plume radius and mass flux increase, in the latter one they decrease down to zero (excluding fluctuations induced by the fact that also momentum goes to zero).

- Plume density, temperature and mass fractions. Integral models predict a

Kinematic decoupling

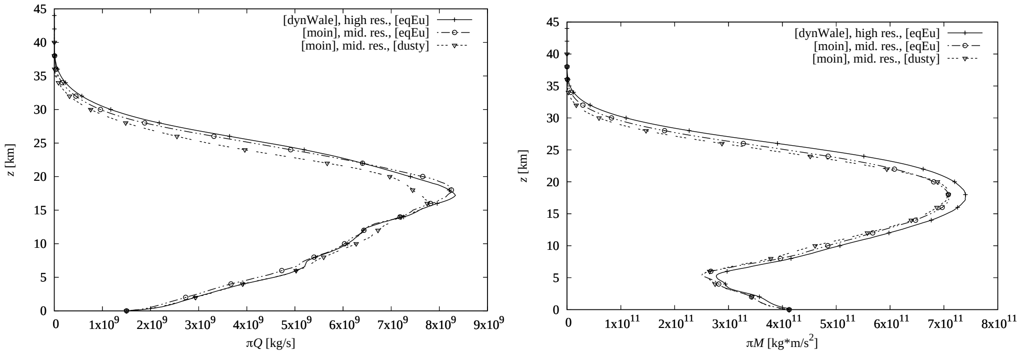

(a) Mass flow rate

(b) Momentum flow rate

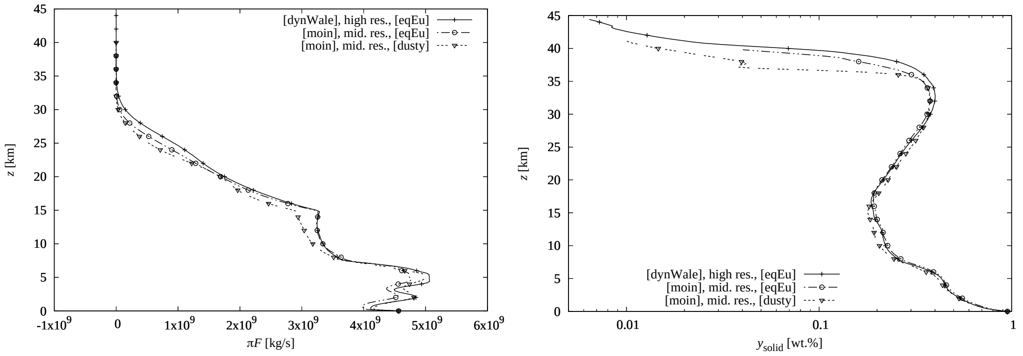

(c) Enthalpy flow rate

(d) Solid mass fraction

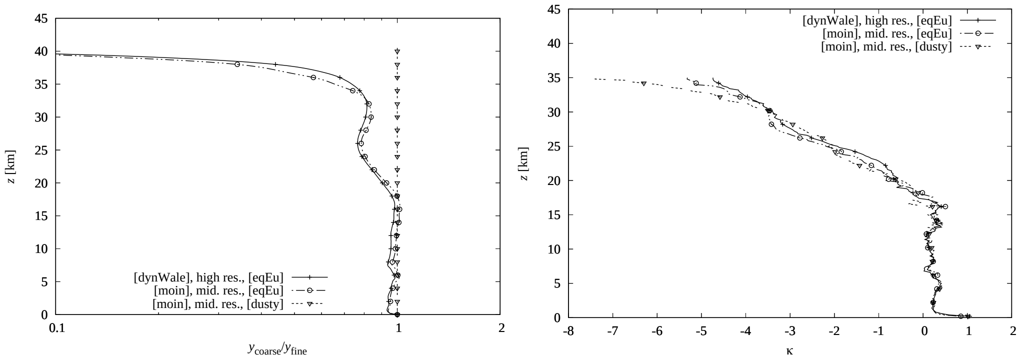

(e) Ratio of coarse on fine mass fractions

(f) Entrainment coefficient

Figure 14: (First part) Influence of the kinematic decoupling model on the profiles of the integral variables of SP. Here we compare results obtained using the [eqEu] model with those from the [dusty] model. The former is reported in the high and middle resolution case, whereas the latter in the middle resolution case.

Kinematic decoupling

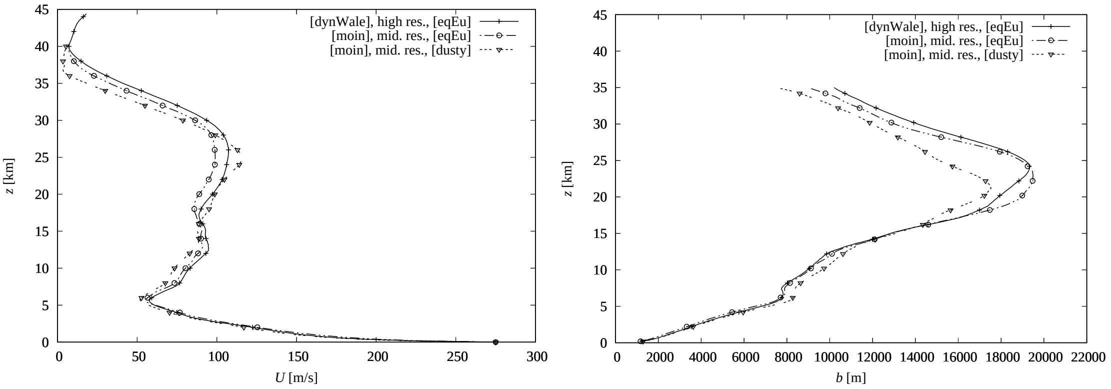

(g) Plume vertical velocity (h) Plume radius

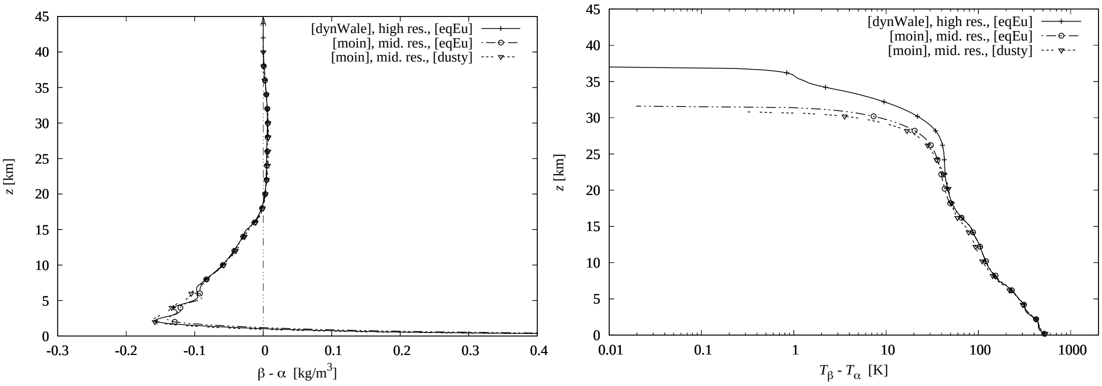

(i) Density difference (j) Temperature difference

Figure 14: (Second part).

slower dilution with respect to the 3D simulation, in particular in the jet region.

- Ejected mixture mass flux. The fluxes Q_e, Q_s defined in Sect. Appendix C are not constant in 3D simulations, while they are constant in integral models.

In the SP, as in the WP eruption, the main source of discrepancy between the 3D solution and the integral one appears to be the entrainment model and the partial collapse dynamics in the jet region. In the 3D simulation we have found an entrainment coefficient larger than that used in the integral model. This means that the integral plume model is diluting much slowly than in 3D simulations, the temperature remains higher, the velocity is larger and the plume goes higher, reaching a NBL 36% higher than that provided by 3D simulations. As in the WP case, above the NBL, assuming a constant entrainment coefficient leads to a wrong behavior, where the plume radius diverges instead of going to zero. This discrepancy adds another source of error to the plume description, which however goes in an opposite direction, decreasing the plume height.

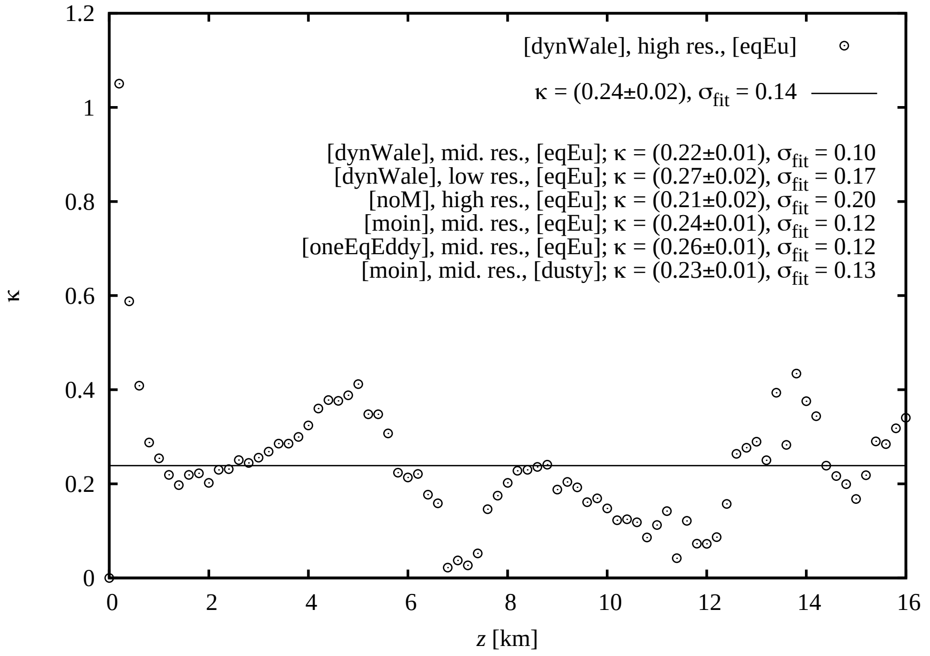

Figure 15: Entrainment coefficient $\varkappa$ of SP below the NBL: $0 \div 16$ km. This is a zoom of Fig. 12f. We show the fit graph obtained at high resolution with the [dynWale] subgrid model, and report in the legend the fit result for the other simulations performed.

Plume conserved quantities. In Fig. 16 we show the behavior of the first integrals of motion in the 3D simulations of the SP. As for the WP eruption, even in the SP we observe that some of the plume parameters have to be modified to obtain the behavior predicted by integral models. In particular, the conservation of the first integral $\mathcal{U}_{\mathrm{RS}}$ requires that the parameter a_q is increased significantly (see Fig. 16). In this way, the evolution of m approximately follows the prediction of integral models, from the vent elevation to the NBL (where m reaches its maximum). However, in the jet region the linear fit is worst than in the WP. As observed in WP, $\mathcal{U}_{\mathrm{RS}}$ is not conserved above the NBL. By increasing slightly γ_{c}, $\mathcal{U}_m$ can be considered approximately constant all along the plume height, even during the buoyancy transition at the NBL. However, as for the WP eruption, in the region near the vent $\mathcal{U}_m$ is subject to a sudden change that we identify in Fig. 16 with $\Delta\mathcal{U}_m \simeq -0.2$. Also in this case, the main motivation can be found in the complex 3D jet structure of the plume near the vent, where the self-similarity assumption is not satisfied.

6. Discussion and Conclusions

6.1. Quality and reliability of Large-Eddy Simulation

The Large Eddy Simulation of volcanic plumes is a challenging task because it requires that the numerical model not only describes the main physical processes occurring in the gas–particle eruptive mixture but also that the most relevant dynamic scales of the turbulence are resolved. In addition, since the

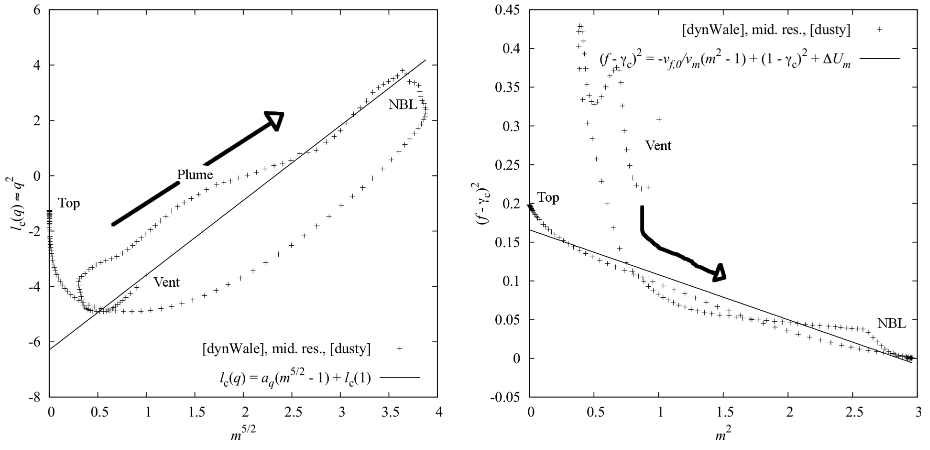

Figure 16: Behavior of conserved quantities of the integral model as calculated from 3D simulations of the SP scenario. Here we modified some of the non-dimensional plume parameters introduced in Appendix C.2 to obtain a better behavior of the conserved quantities (see discussion): $a_q = 0.473 \to a_q = 2.7$, $\gamma_c = 0.345 \to \gamma_c = 0.445$. Moreover, we used the value of $v_{f,0} = 3.0 * 10^{-2}$ obtained averaging the atmospheric profile: $\mathcal{N}_0 \simeq 2.61 * 10^{-2}$ Hz. The arrows indicate the versus of the flow in the plume, from the vent to the NBL.

transport equations are non-linear, the unresolved (subgrid) scales need in general to be modeled to properly describe their effect on the large-eddy scales of motion and avoid either the accumulation of energy in the high-frequency fluctuations or the excessive numerical diffusion. This is critical in the LES of volcanic plumes because the large-eddy scales controlling the entrainment rate are usually at the threshold between grid-resolved and subgrid scales.

The numerical discretization and solution approach adopted by the ASHEE model has demonstrated in several benchmarks (Cerminara et al., 2016) the ability to accurately reproduce the turbulent spectrum in both Direct and Large-Eddy Simulation. In particular, the model is able to reproduce not only the averaged dynamics of a laboratory forced plume but also the statistics of turbulent fluctuations, controlling the mixing rate. Such results are encouraging and strongly support the reliability of the adopted numerical model for volcanic plume simulation. However, it is worth recalling that volcanic plumes are characterized by a Reynolds number several orders of magnitude larger than a laboratory plume and that atmospheric stratification strongly characterizes volcanic plume dynamics, making an exact scaling of laboratory and DNS experiments extremely difficult. Despite these limitations, we have demonstrated in this work (Fig. 10 and 11) that high-resolution numerical simulations are able to reproduce some qualitative and quantitative features of the infrasonic spectrum emitted by volcanic plumes, an observable strictly linked to the (compressible) turbulent regime.

On the other hand, we have also shown (Figs. 4 and 12–14) that low- and mid-resolution LES are able to capture the essential features of high-resolution simulations, predicting consistent averaged flow fields. In particular, the uncertainty on the averaged flow fields associated with the adopted grid resolutions and subgrid models is significantly lower than that related to the the choice of the entrainment coefficient in integral models (see results of the intercomparison study presented in Costa et al., 2016, this issue). In particular, the limited effect associated with the choice of the SGS model is well shown in Figs. 13g, 13h. The larger effect is associated to the presence of the SGS model itself (which improves the accuracy and the stability of the simulation). When SGS models are used, the differences between dynamic and static models are of second-order importance. As a consequence, a first-order description of the mean properties of volcanic plumes can be achieved without the need of any empirical constant in the modeling of the turbulence.

For what concerns fluctuation properties, we have indications that the effect of grid resolution and SGS model is relevant, although we have not carried out a detailed study on this aspect. This is suggested, for example, by the measure of the variations around the mean value of the entrainment coefficient, below the NBL (Figs. 5 and 15).

6.2. Non-equilibrium gas–particle effects

In this work, we have analyzed the net effect on the mean flow profiles obtained by switching on and off the kinematic decoupling terms in the transport equations. Such an effect is larger in the WP than in the SP because the particle Stokes number of the coarsest particles is larger in the former (0.1, with respect to 0.06). For the WP case, the effect of the gas–particle decoupling is significantly larger than the effect of the considered mesh resolutions (Figs. 4g, 4h). Consistently with the lower Stokes number, such an effect is less evident for the SP case. We have shown that particle non-equilibrium introduces a novel phenomenon, that we have called jet-dragging, clearly observable in the WP case. Because of the kinematic decoupling, all profiles are shifted up (by about 20-25% in the present application) in the non-equilibrium case. In addition, non-equilibrium effects increase the radius in the buoyant plume region of about 20%. This reflects systematically in the umbrella region, which is much depleted of particles in the dusty gas model (around 10% of the total plume height in the WP case).

We have not carried out a detailed study on the effect the non-equilibrium on fluctuations. However, this is clearly important, at least for coarse particles, as highlighted by the instantaneous particle distribution in the plume (Figs. 3a, 9a). In the WP, preferential concentration ranges between 0.05 and 5, i.e., density fluctuates by up to two orders of magnitude due to clustering. In the SP case, this range reduces to $0.1 \div 2$.

6.3. Comparison with integral models

The comparison of the averaged plume variables from the LES model and results of integral models allowed us to quantitatively estimate the quality of the 1D approximation. In the WP case, 3D results are consistent with the predictions of integral models in the jet and plume regions, with an entrainment coefficient around 0.10 in the plume region below the NBL. In the SP case, the 1D approximation results less appropriate and the calculated entrainment coefficient in the plume region is more unstable, with an higher average value equal to 0.24. In both cases, integral models predictions diverge from the 3D plume behavior in the umbrella region, where the entrainment coefficient assumes negative values.

The main discrepancies between 1D and 3D model results derive from the different entrainment model. In the WP case, three dimensional simulations conserve the first integrals of motion predicted by integral models. However, one of these integrals depends on the entrainment coefficient and needs to be corrected, suggesting that the entrainment model has to be better calibrated. On the contrary, in the SP case, it is not possible to calibrate an entrainment coefficient to conserve the integral. This suggests that the entrainment in presence of a fountain-like or partial column collapse structure should to be expressed by a more complex functional form.

On the other hand, the second integral of motion does not depend on the entrainment assumption. This allowed us to test the consistency of the 1D approximation beyond the entrainment hypothesis. Such integral is almost perfectly conserved above the gas thrust region in both test cases. This suggests that an important source of discrepancy between 1D and 3D models is the self-similarity approximation of the horizontal profiles in the lower region.

Finally, we comment about the resulting plume height and NBL. Predictions of the LES model differ from those of integral models. In the WP case, both levels are underestimated by about 10% mainly because of the entrainment assumption in the jet region. In the SP case, the NBL is strongly overestimated by integral models, indicating that the assumptions behind integral models are weaker both in the jet and plume region. For both cases, integral models description of the umbrella region is not appropriate: for the integral models the entrainment remains constant and positive, while in 3D simulations it varies largely and becomes negative. In the SP, this effect counterbalances the higher NBL making the total plume height quite consistent with 3D results. Our ASH0D approximation works satisfactorily well (with respect ASH1D), capturing both mean profiles and plume heights (Figs. C.17 and C.18).

6.4. Future directions

Present results confirm that, when the grid resolution of the LES is fine enough (roughly, at least ten cells in the vent diameter, as firstly suggested by Suzuki et al., 2005), any strong influence of grid resolution and subgrid model can be excluded. However, a much detailed analysis on the use of non-diffusive shock–capturing schemes (as recently proposed for example by Vuorinen et al., 2013) is necessary to further reduce the influence of numerical error in supersonic regimes.

From the present study, we have shown that non-equilibrium gas–particle effects should have a second-order influence on the dynamics of the analyzed regimes. As a further development, the coarsest portion of the grain size distribution (above about 1 mm) will be included in the model by means of Lagrangian techniques.

The present study demonstrates that Large Eddy Simulation can reliably describe the dynamics of volcanic plumes and are an irreplaceable tool to identify the critical hypotheses and to calibrate empirical parameters at the base of integral models used in operational studies. In addition, they allow to study unexplored regimes where integral model assumptions are flawed and provide the unprecedented capability to reproduce observables quantities (such as infrasound signals) which can be useful to constrain eruption dynamics in real cases. Future works shall be expressly devoted to improving the comparison between observational/laboratory data and numerical results (Cerminara et al., 2015).

Finally, to consider more realistic volcanological scenarios, more complex atmospheric conditions including wind and the volcano topography will be added by exploiting the capability of ASHEE of using non-structured hexahedral meshes. This will also allow to derive an effective entrainment coefficient in case of wind (including the cross-wise coefficient Bursik, 2001) and to study the gravity current above the NBL, exploiting the 3D simulations to calibrate simple 1D gravity current models (e.g. Suzuki and Koyaguchi, 2009; Costa et al., 2013).

Appendix A. Table of symbols

$\boldsymbol{a}$	acceleration vector field
b	plume radius
C	specific heat at constant pressure
C_v	specific heat at constant volume
$\mathcal{C}_j$	jth particle concentration relative to that of a tracer
d	particle diameter
D	vent diameter
$\mathfrak{f}$	generic field
f	non-dimensional enthalpy flux
F	enthalpy (buoyancy) flux divided by π
$\boldsymbol{g}$	gravity acceleration
h	enthalpy
H	plume height
i	index running over all the gas phases
I	number of gas phases
$\mathcal{I}$	set of all indexes i
j	index running over all the solid phases
J	number of solid phases (particle classes)
$\mathcal{J}$	set of all indexes j
K	kinetic energy
L	integral length scale of the domain Ω
m	non-dimensional momentum flux
M	momentum flux divided by π
$\mathcal{N}_0$	mean Brunt-Väisälä frequency
p	pressure
Pr	Prandtl number
q	non-dimensional mass flux
$\boldsymbol{q}$	heat flux
Q	mass flux divided by π
R	gas constant
Re	Reynolds number
S	source term
St	Stokes number
Str	Strouhal number
t	time
T	temperature
$\mathcal{T}$	temporal domain

$\mathbb{T}$	stress tensor
$\mathbb{T}_\mathrm{r}$	kinematic decoupling tensor
$\boldsymbol{u}$	velocity vector
U	plume axial velocity
$\mathcal{U}$	quantity conserved along the plume axis by integral models
$\boldsymbol{v}$	relative velocity field
V	volume
$\boldsymbol{w}$	settling velocity
$\boldsymbol{x}$	spatial coordinate
y	mass fraction
Y	horizontally averaged mass fraction
z	vertical coordinate
$\hat{z}$	vertical versor
α	atmospheric density
β	plume density
γ_c	column stability
δ	minimum grid size
ϵ	volume concentration
η	Kolmogorov length scale
$\varkappa$	entrainment coefficient
λ_T	Taylor microscale
μ	dynamic viscosity
ν	kinematic viscosity
ξ	LES resolved spatial scale
ρ	bulk density
$\hat{\rho}$	density
τ	typical time scale
τ_η	Kolmogorov time scale
υ	molar fraction
χ	non-dimensional specific heat
ψ	non-dimensional gas constant
Ω	spatial domain
$(\cdot)_0$	at the vent level
$(\cdot)_\mathrm{g}$	of the gas phase
$(\cdot)_i$	of the ith gas component
$(\cdot)_j$	of the jth solid phase
$(\cdot)_k$	of the kth generic phase or component
$(\cdot)_\mathrm{m}$	of the mixture
$(\cdot)_\mathrm{nbl}$	at the plume neutral buoyancy level
$(\cdot)_\mathrm{s}$	of the solid phase
$(\cdot)_\mathrm{top}$	at the plume top
$(\cdot)_\alpha$	of the atmosphere
$(\cdot)_\beta$	of the plume

Appendix B. The ASHEE model equations

Balance equations. The balance equations of mass, momentum, and enthalpy of a multiphase mixture of I gas components and J solid particulate phases in "mixture" formulation are (see Cerminara et al., 2016):

$$\partial_t \rho_\mathrm{m} + \nabla\cdot(\rho_\mathrm{m}\boldsymbol{u}_\mathrm{m}) = \sum_j S_j \tag{B.1a}$$

$$\partial_t(\rho_\mathrm{m} y_i) + \nabla\cdot(\rho_\mathrm{m}\boldsymbol{u}_\mathrm{g} y_i) = 0\,, \quad i\in\mathcal{I} \tag{B.1b}$$

$$\partial_t(\rho_\mathrm{m} y_j) + \nabla\cdot[\rho_\mathrm{m}(\boldsymbol{u}_\mathrm{g}+\boldsymbol{v}_j) y_j] = S_j\,, \quad j\in\mathcal{J} \tag{B.1c}$$

$$\begin{aligned}&\partial_t(\rho_\mathrm{m}\boldsymbol{u}_\mathrm{m}) + \nabla\cdot(\rho_\mathrm{m}\boldsymbol{u}_\mathrm{m}\otimes\boldsymbol{u}_\mathrm{m} + \rho_\mathrm{m}\mathbb{T}_\mathrm{r}) + \nabla p = \\ &\qquad\qquad = \nabla\cdot\mathbb{T} + \rho_\mathrm{m}\boldsymbol{g} + \sum_j S_j\boldsymbol{u}_j\end{aligned} \tag{B.1d}$$

$$\begin{aligned}&\partial_t(\rho_\mathrm{m} h_\mathrm{m}) + \nabla\cdot[\rho_\mathrm{m} h_\mathrm{m}(\boldsymbol{u}_\mathrm{m}+\boldsymbol{v}_h)] = \\ &\quad = \partial_t p - \partial_t(\rho_\mathrm{m} K_\mathrm{m}) - \nabla\cdot[\rho_\mathrm{m} K_\mathrm{m}(\boldsymbol{u}_\mathrm{m}+\boldsymbol{v}_K)] + \\ &\qquad + \nabla\cdot(\mathbb{T}\cdot\boldsymbol{u}_\mathrm{g} - \boldsymbol{q}) + \rho_\mathrm{m}(\boldsymbol{g}\cdot\boldsymbol{u}_\mathrm{m}) + \sum_j S_j(h_j + K_j)\end{aligned} \tag{B.1e}$$

where ρ_m, $\boldsymbol{u}_\mathrm{m}$, and h_m are the mixture density, velocity, and enthalpy, respectively. The velocity fields of the gas and of the solid phases are $\boldsymbol{u}_\mathrm{g}$ and $\boldsymbol{u}_j \equiv \boldsymbol{u}_\mathrm{g} + \boldsymbol{v}_j$, so that $\boldsymbol{v}_j$ is the relative velocity field between the jth solid phase and the gas phase. The mass fractions of the gas and solid phases are denoted by y_i and y_j, respectively. Eq. (B.1a) is redundant, since it is just the sum of Eqs. (B.1b) and (B.1c) (recall $\sum_\mathcal{I} y_i + \sum_\mathcal{J} y_j = 1$). The terms which are present also in the single phase formulation of the compressible Navier-Stokes equations depend on: the pressure field of the gas phase p; the stress tensor field of the gas phase $\mathbb{T}$; the gravity acceleration $\boldsymbol{g}$; the kinetic energy per unity of mass of the mixture $K_\mathrm{m} = \sum_\mathcal{I} y_i K_i + \sum_\mathcal{J} y_j K_j$, $K \equiv \frac{1}{2}|\boldsymbol{u}|^2$; the heat flux in the gas mixture $\boldsymbol{q}$. The term S_j is the source (sink) term relative to the jth solid phase. The terms $\mathbb{T}_\mathrm{r}$, $\boldsymbol{v}_h$, and $\boldsymbol{v}_K$ are those keeping into account the effect of kinematic decoupling between the phases in the mixture. The effect of a possible thermal disequilibrium is kept in the field $h_\mathrm{m} = \sum_\mathcal{I} y_i h_i + \sum_\mathcal{J} y_j h_j$.

The system of equations (B.1) is not closed. The following constitutive equations are needed: $p = p(\rho_\mathrm{m}, T_\mathrm{g})$, $\mathbb{T} = \mathbb{T}(\boldsymbol{u}_\mathrm{m}, T_\mathrm{g})$, $h_i = h_i(T_\mathrm{g})$, $h_j = h_j(T_j)$, $\boldsymbol{q} = \boldsymbol{q}(T_\mathrm{g})$; where T_g and T_j are the temperature fields of the gas phase and of the jth solid phase, respectively. Moreover, additional information are needed for the determination of the kinematic and thermal decoupling terms $\boldsymbol{v}_j$ and $T_j - T_\mathrm{g}$. All these information for the ASHEE model are summarized in the next section.

Constitutive equations. The ASHEE model uses the ideal gas hypothesis in the volume occupied by the gas phase. The corresponding constitutive equation can be written starting from $p = \sum_\mathcal{I} \hat{\rho}_i R_i T_\mathrm{g}$:

$$\frac{1}{\rho_\mathrm{m}} = \sum_j \frac{y_j}{\hat{\rho}_j} + \sum_i \frac{y_i R_i T_\mathrm{g}}{p}\,, \tag{B.2}$$

R_i being the gas constant of the ith component.

The stress tensor is related by a classical relationship to the rate-of-shear $\mathbb{S}_\mathrm{g}$ and the strain-rate $\mathbb{D}_\mathrm{g} = \mathrm{Sym}(\nabla\boldsymbol{u}_\mathrm{g})$ tensors:

$$\mathbb{T} = 2\mu\,\mathbb{S}_\mathrm{g} \tag{B.3}$$

$$\mathbb{S}_\mathrm{g} = \mathbb{D}_\mathrm{g} - \frac{1}{3}\mathrm{Tr}(\mathbb{D}_\mathrm{g})\,\mathbb{I}\,. \tag{B.4}$$

Here μ is the dynamic viscosity of the gas phase, defined knowing the viscosity of each gas component μ_i and its molar fraction υ_i:

$$\mu = \sum_i \upsilon_i \mu_i \,. \tag{B.5}$$

In ASHEE, the dynamic viscosity of the gaseous component can be considered constant or depending on the temperature by the Sutherland law:

$$\mu_i = \mu_i(T_\mathrm{g}) = \frac{\mu_\mathrm{Sth}\, T_\mathrm{g}^{\frac{3}{2}}}{T_\mathrm{g} + T_\mathrm{Sth}} \,, \tag{B.6}$$

where μ_Sth and T_Sth are two constants depending on the fluid. Using data from the NIST Chemistry WebBook, we got results presented in Tab. B.2. In the simulations presented here we used a constant value for the viscosity, as requested in the IAVCEI intercomparison study.

fluid	temperature interval	μ_Sth	T_Sth
air	$100 \div 1500\,\mathsf{K}$	$(1.5697 \pm 0.0009) * 10^{-6}\,\mathsf{Pa\,s}$	$(144 \pm 1)\,\mathsf{K}$
steam	$375 \div 1275\,\mathsf{K}$	$(2.528 \pm 0.003) * 10^{-6}\,\mathsf{Pa\,s}$	$(1130 \pm 2)\,\mathsf{K}$

Table B.2: Sutherland law constants obtained by fitting data from NIST Chemistry WebBook `http://webbook.nist.gov/chemistry/fluid/`.

As usually done, the heat flux $\boldsymbol{q}$ is defined through the Fourier law

$$\boldsymbol{q} = -k_\mathrm{g}\, \nabla T_\mathrm{g} \,, \tag{B.7}$$

while the particle-particle heat flux has been disregarded because negligible in dispersed multiphase turbulence ($\epsilon_\mathrm{s} \lesssim 10^{-3}$). We define the gas phase Prandtl number:

$$\mathrm{Pr}_\mathrm{g} = \frac{\mu\, C_\mathrm{g}}{k_\mathrm{g}} \,. \tag{B.8}$$

Throughout this work, we will use for atmospheric air the assumption $\mathrm{Pr}_\mathrm{g} = 0.71$, as a good approximation of the temperature dependence of the thermal conductivity on temperature (Garnier et al., 2009). Here C_g is the specific heat at constant pressure and k_g is the thermal conductivity of the gas phase.

Finally, defining $C_{\mathrm{v},i}$ and $C_{\mathrm{v},j}$ the specific heats at constant volume of the ith gas component and of the jth phase, the enthalpy is related to the temperature through the following relations:

$$h_i = C_{\mathrm{v},i} T_\mathrm{g} + p/\rho_\mathrm{g} \tag{B.9}$$

$$h_j = C_{\mathrm{v},j} T_j \tag{B.10}$$

so that $\sum_\mathcal{I} y_i h_i = y_\mathrm{g} h_\mathrm{g}$, $h_\mathrm{g} = \sum_i \rho_i C_{\mathrm{v},i} T_\mathrm{g}/\rho_\mathrm{g} + p/\rho_\mathrm{g}$, and

$$h_\mathrm{m} = \sum_i y_i C_{\mathrm{v},i} T_\mathrm{g} + \sum_j y_j C_{\mathrm{v},j} T_j + \frac{p}{\rho_\mathrm{m}} \,. \tag{B.11}$$

Decoupling: the Equilibrium–Eulerian approach. Kinematic decoupling is resolved in ASHEE by using the Equilibrium–Eulerian model (see Ferry and Balachandar, 2001; Ferry et al., 2003; Balachandar and Eaton, 2010; Cerminara et al., 2016). The full momentum balance equations of the jth solid phase can be explicitly solved if $\mathrm{St}_j < 0.2$. The asymptotic solution is

$$\boldsymbol{v}_j = \boldsymbol{u}_j - \boldsymbol{u}_\mathrm{g} = \boldsymbol{w}_j - \tau_j(\boldsymbol{a}_\mathrm{g} + \boldsymbol{v}_j \cdot \nabla \boldsymbol{u}_\mathrm{g}) + O(\tau_j^2)\,, \tag{B.12}$$

where $\boldsymbol{w}_j = \tau_j \boldsymbol{g}$ is the settling velocity and

$$\tau_j = \frac{\hat{\rho}_j\, d_j^2}{18\mu\, \phi_\mathrm{c}} \tag{B.13}$$

$$\phi_\mathrm{c} = 1 + 0.15\, \mathrm{Re}_j^{0.687}\,. \tag{B.14}$$

The function $\phi_\mathrm{c}(\mathrm{Re}_j)$ corrects the Stokes time τ_j in the regime $1 < \mathrm{Re}_j < 1000$ for spherical particles. The introduction of alternative empirical corrections is straightforward. In Cerminara (2016) we showed that the relative Reynolds number between the jth solid phase and the gas phase

$$\mathrm{Re}_j = \frac{\hat{\rho}_\mathrm{g} d_j |\boldsymbol{v}_j|}{\mu}\,, \tag{B.15}$$

can be evaluated directly with

$$\mathrm{Re}_j = \frac{\mathrm{Re}_j^*}{1 + 0.315\,(\mathrm{Re}_j^*)^{0.4072}}\,, \quad \text{where} \quad \mathrm{Re}_j^* \equiv \frac{\hat{\rho}_\mathrm{g}\hat{\rho}_j d_j^3 |\boldsymbol{g} - \boldsymbol{a}_\mathrm{g}|}{18\mu^2}\,. \tag{B.16}$$

Thermal decoupling is disregarded in ASHEE, because Ferry and Balachandar (2005) and Cerminara et al. (2016) demonstrated that the error made by assuming thermal equilibrium is at least one order of magnitude smaller than kinematic one. Thus $T_j = T_\mathrm{g} = T$ and

$$h_\mathrm{m} = C_{\mathrm{v,m}} T + \frac{p}{\rho_\mathrm{m}} \tag{B.17}$$

$$C_{\mathrm{v,m}} = \sum_i y_i C_{\mathrm{v},i} + \sum_j y_j C_{\mathrm{v},j}\,. \tag{B.18}$$

LES formulation and Sub-grid scale modeling. The model equations described above should be filtered in order to obtain the LES formulation, leading to additional terms accounting for eddy diffusivity terms and for the sub-grid scale Reynolds stress. The procedure is detailed by Cerminara et al. (2016); Cerminara (2016).

Appendix C. Integral plume models

Appendix C.1. The ASH1D model

We here describe the ASH1D model of volcanic plumes adopted for this study, whose results are presented in Figs. C.17 and C.18, and also discussed in the intercomparison paper by Costa et al. (2016). The model rewrites the Woods (1988) model in a compact form, as a closed system of ordinary differential equations (including the thermodynamics of the gas–particle mixture). The model is written for a gas–particle volcanic plume composed, at the vent, by two phases: the solid particles $(\cdot)_\mathrm{s}$ and the ejected gas phase $(\cdot)_\mathrm{e}$. They can be derived directly from the dusty-gas model in 3D by assuming a number of additional hypothesis. The full derivation can be found in Cerminara (2015). In the dilute approximation, ASH1D is equivalent to Woods (1988), i.e. it predicts the evolution of Q, M and F (defined by Eqs. (17)) along the plume axis.

$$Q' = 2U_\epsilon(\alpha, Q, M, F)\sqrt{\frac{\alpha Q(F+Q)(Q+Q_\psi)}{M[Q+Q_\chi]}} \tag{C.1a}$$

$$M' = \frac{gFQ}{M}\left[1 - \frac{(F+Q)(Q_\chi - Q_\psi)}{F[Q+Q_\chi]}\right] \tag{C.1b}$$

$$F' = -(F+Q)\frac{(C_\alpha T_\alpha)'}{C_\alpha T_\alpha} + \frac{M^2 Q'}{2C_\alpha T_\alpha Q^2} - \frac{g(F+Q)(Q+Q_\psi)}{C_\alpha T_\alpha (Q+Q_\chi)}\,. \tag{C.1c}$$

To obtain the result, Eqs. (18) are needed, with the definition of Q_χ, Q_ψ, F and the entrainment velocity U_ϵ. The two mass fluxes take into account the multiphase nature of the fluid:

$$Q_\psi = -Q_\mathrm{s} + (\psi_\mathrm{e} - 1)Q_\mathrm{e}\,, \tag{C.2}$$

$$Q_\chi = (\chi_\mathrm{s} - 1)Q_\mathrm{s} + (\chi_\mathrm{e} - 1)Q_\mathrm{e}\,, \tag{C.3}$$

and are constant in the whole plume height ($Q'_\psi = 0$, $Q'_\chi = 0$). Coherently with that reported in Eqs. (18) and (17), the mass fractions $Y_\psi = Q_\psi/Q$ and $Y_\chi = Q_\chi/Q$, as well as the enthalpy flux

$$F = \left[(\alpha - \beta) + \alpha\frac{Q_\chi - Q_\psi}{Q + Q_\psi}\right] Ub^2\,, \tag{C.4}$$

can be derived from the thermodynamics of the plume mixture (see Cerminara, 2015). In ASH1D, we model the entrainment velocity as done by Woods (1988): we use the Ricou and Spalding (1961) model

$$U_\epsilon/U = \varkappa\sqrt{\beta/\alpha} \tag{C.5}$$

below the jet-plume transition level, and the Morton et al. (1956) model ($U_\epsilon/U = \varkappa$) above.

Appendix C.2. The ASH0D model

In Cerminara (2015, 2016), an approximated analytical solution of the ASH1D model (C.1) is presented. In Cerminara et al. (2015) this solution is applied to a real volcanic eruption. In this paper we refer to this analytical approximation as ASH0D.

To obtain the ASH0D solution, three main steps were carried out:

- System (C.1) has been written in non-dimensional form, with respect to the value at the vent of the fluxes $q = Q/Q_0$, $m = M/M_0$ and $f = F/F_0$. The non-dimensional level $\zeta = z/\ell_0$ is defined on the basis of these fluxes: $\ell_0 = Q_0/\sqrt{\alpha_0 M_0}$. The importance of the density contrast at the vent is measured by $\phi = F_0/Q_0$, while the fountain stability is measured by

$\gamma_\mathrm{c} = (Q_\chi - Q_\psi)/F_0$. The multiphase nature of the plume is measured by $q_\chi = Q_\chi/Q_0$ and $q_\psi = Q_\psi/Q_0$.

The parameters measuring the degree of variation of q, m, and f are respectively v_q, v_m and $v_{f,0}$. The first is nothing but twice $\varkappa$, the second is the Richardson number $v_m = gF_0Q_0\ell_0/M_0^2$, and the third is the non-dimensional ambient stratification $v_{f,0} = Q_0\ell_0\mathcal{N}_0^2/gF_0$. $\mathcal{N}_0$ is the mean Brunt-Väisälä frequency. We set it to $\mathcal{N}_0 = 1.13 * 10^{-2}\,\mathsf{Hz}$.

- A generalization to the multiphase case of the asymptotic solution written by Morton et al. (1956) has been found:

$$q(\zeta) = \left(\frac{3v_q}{5a_q^{1/5}}\,\zeta + 1\right)^{\frac{5}{3}}, \qquad a_q = \frac{4v_q}{5v_m(1-\gamma_\mathrm{c})}. \tag{C.6}$$

- Two first-integral of motion have been found: $\mathcal{U}_\mathrm{RS}$ and $\mathcal{U}_m$. The functional form of the first does depend on the entrainment model used (namely, Ricou and Spalding, 1961), while the second does not. In particular, they are:

$$\mathcal{U}_\mathrm{RS} = l(q) - \frac{4v_q}{5v_m}m^{5/2} = l(1) - \frac{4v_q}{5v_m} \tag{C.7}$$

$$\mathcal{U}_m = (1-\gamma_\mathrm{c})^2 + \frac{v_{f,0}}{v_m} = (f-\gamma_\mathrm{c})^2 + \frac{v_{f,0}}{v_m}m^2\,, \tag{C.8}$$

where

$$l(q) = q^2(1-\gamma_\mathrm{c}) - 2\gamma_\mathrm{c}(\phi - q_\chi)\left[q - q_\chi\ln(|q+q_\chi|)\right] \approx q^2 \tag{C.9}$$

takes into account the density contrast and the composition of the plume.

By assembling all the elements here described, the profiles $Q(z)$, $M(z)$ and $F(z)$ can be constructed. By using Eqs. (18), all the dependent variables can be obtained from the initial conditions.

Finally, $\mathcal{U}_m$ can be used to evaluate H_top and H_nbl. Indeed, at $z = H_\mathrm{nbl}$ the momentum flux reaches its maximum (thus $f_\mathrm{nbl} = \gamma_\mathrm{c}$), while at $z = H_\mathrm{top}$ it falls to zero (thus $f_\mathrm{top} = \gamma_\mathrm{c} - \sqrt{\mathcal{U}_m}$).

Weak and Strong plume solutions. The behavior of the ASH0D approximation with respect to ASH1D and ASHEE (executed in [dusty] regime, for coherence with integral models) is showed in Figs. C.17, C.18, for the WP and SP cases, respectively. We notice that the approximated solution works surprisingly well for both the presented plumes. In particular, the temperature and density profiles are well captured for both cases. The best behavior is observed for the WP case.

Comments on the comparison between integral and 3D models are in Sects. 4.3 (WP) and 5.3 (SP). On the other hand, by comparing ASH0D with ASH1D, we notice that the asymptotic solution behaves worse for the plume radius and the plume axial velocity in the upper part, where the stratification plays the most important role. Anyway, the plume maximum height is captured with less than 12% of error for both the plumes. The NBL of the SP has a larger error because of the jet region, where the enthalpy flux increases. Systematically, the asymptotic mass flux is overestimated with respect to ASH1D. This error occurs with more evidence in the SP case, and directly reflects in the underestimation of the mass fractions along the plume axis. However for all the presented profiles, the distance between ASH0D and ASH1D is smaller or of the same order of the distance between ASH1D and ASHEE.

Acknowledgments. This work includes some results achieved in the PhD work by the first author (MC), carried out at Scuola Normale Superiore, Pisa, with a grant by Istituto Nazionale di Geofisica e Vulcanologia. MC is member of GNAMPA, of the Istituto Nazionale di Alta Matematica "F. Severi". MC was partially supported by the European MED-SUV project. We acknowledge the CINECA for the availability of high-performance computing resources and technical support on porting OpenFOAM® on HPC architectures by I. Spisso and M. Culpo. In particular, this work took advantage of the CINECA infrastructure through the ISCRA projects: IsB06 VolcFOAM, IsC26 VolcAshP, IsC35 VolcAshW and IsC07 GEOFOAM. We thank A. Costa and Y. Suzuki together with colleagues involved in the IAVCEI intercomparison study on volcanic plume models for useful discussions and stimulating exchanges. Finally, we thank Arnau Folch and an anonymous reviewer for their comments, which improved the paper quality.

References

Balachandar S, Eaton JK. Turbulent Dispersed Multiphase Flow. Annu Rev Fluid Mech 2010;42(1):111–33. doi:`10.1146/annurev.fluid.010908.165243`.

Bisset D, Hunt JC, Rogers M. The turbulent/non-turbulent interface bounding a far wake. J Fluid Mech 2002;451:383–410. doi:`10.1017/S0022112001006759`.

Bursik MI. Effect of wind on the rise height of volcanic plumes. Geophys Res Lett 2001;28(18):3621–4. doi:`10.1029/2001GL013393`.

Carazzo G, Kaminski É, Tait S. On the rise of turbulent plumes: Quantitative effects of variable entrainment for submarine hydrothermal vents, terrestrial and extra terrestrial explosive volcanism. J Geophys Res 2008;113(B9):B09201. doi:`10.1029/2007JB005458`.

Carcano S, Esposti Ongaro T, Bonaventura L, Neri A. Influence of grain-size distribution on the dynamics of underexpanded volcanic jets. J Volcanol Geotherm Res 2014;285:60–80. doi:`10.1016/j.jvolgeores.2014.08.003`.

Cerminara M. The Multiphase Buoyant Plume Solution of the Dusty Gas Model. ArXiv 2015;`arXiv:1506.01638`.

Cerminara M. Modeling dispersed gas–particle turbulence in volcanic ash plumes. PhD thesis; Scuola Normale Superiore; 2016. To appear.

Cerminara M, Esposti Ongaro T, Berselli LC. ASHEE-1.0: a compressible, equilibrium–Eulerian model for volcanic ash plumes. Geosci Model Dev 2016;9(2):697–730. doi:`10.5194/gmd-9-697-2016`. `arXiv:1509.00093`.

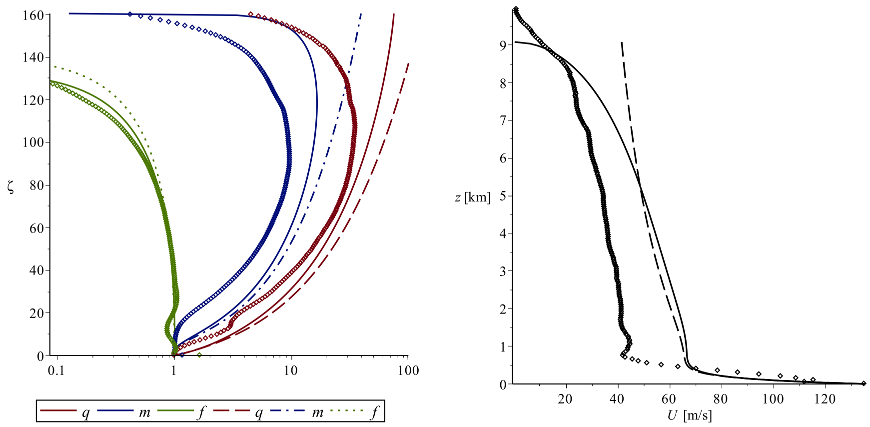

(a) mass, momentum and enthalpy fluxes

(b) axial velocity

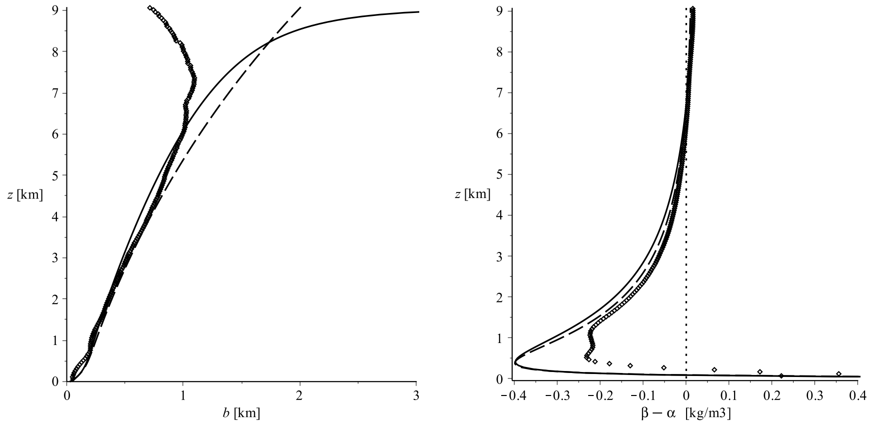

(c) plume radius

(d) density contrast

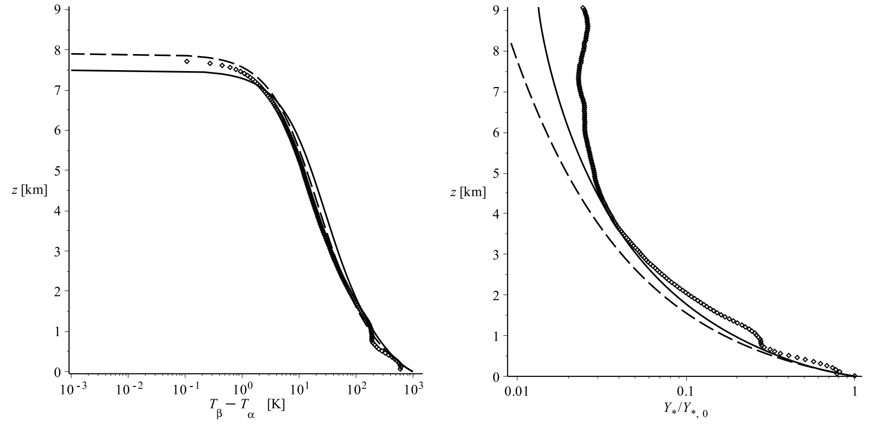

(e) temperature contrast

(f) plume mass fractions

Figure C.17: WP: (a) vertical distribution of the non-dimensional fluxes q, m, f (log-linear scale) and of the dimensional physical parameters (b) U, (c) b, (d) $\beta - \alpha$, (e) $T_\beta - T_\alpha$, and (f) $Y_*/Y_{*,0}$. Solid lines correspond to the numerical solution of ASH1D (C.1), while dashed lines are evaluated by using ASH0D. Points are from ASHEE numerical simulation, in configuration low-res, [dynWale] and [dusty], cf Fig. 4.

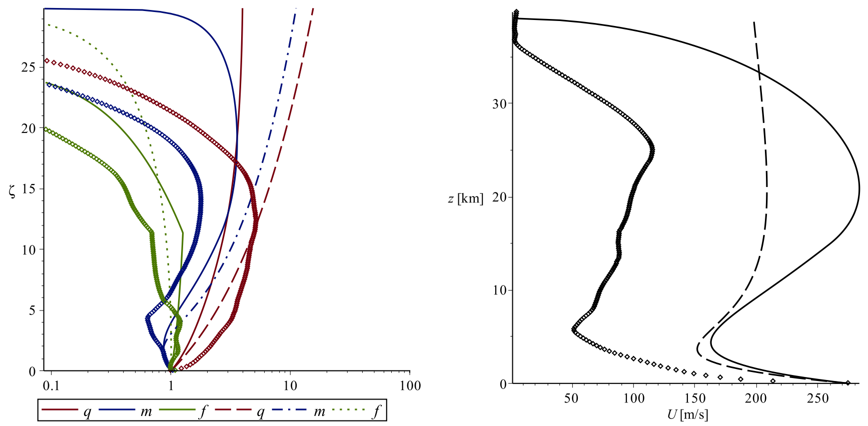

(a) mass, momentum and enthalpy fluxes

(b) axial velocity

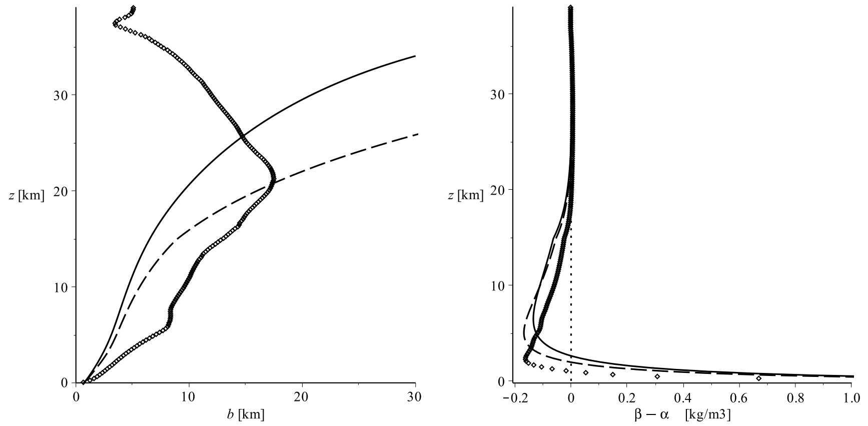

(c) plume radius

(d) density contrast

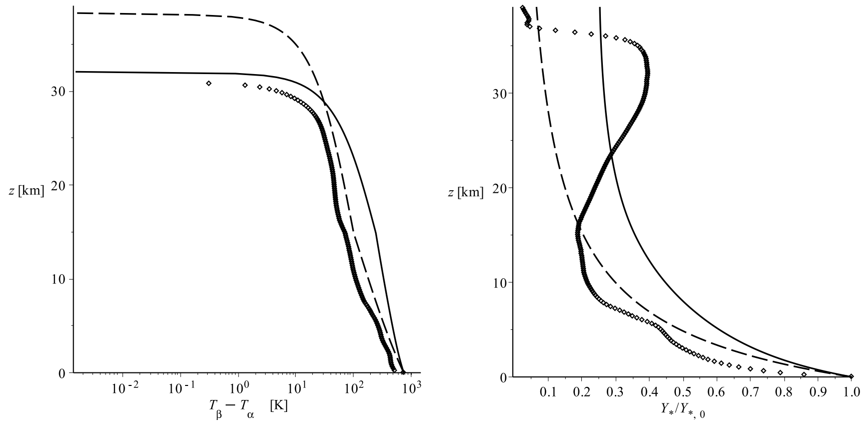

(e) temperature contrast

(f) plume mass fractions

Figure C.18: SP: (a) vertical evolution of the non-dimensional fluxes q, m, f (log-linear scale) and of the dimensional physical parameters (b) U, (c) b, (d) $\beta - \alpha$, (e) $T_\beta - T_\alpha$, and (f) $Y_*/Y_{*,0}$. Solid lines correspond to the numerical solution of ASH1D (C.1), while dashed lines are evaluated by using ASH0D. Points are from ASHEE numerical simulation, in configuration mid-res, [moin], and [dusty], cf. Fig. 14.

Cerminara M, Esposti Ongaro T, Valade S, Harris AJ. Volcanic plume vent conditions retrieved from infrared images: A forward and inverse modeling approach. J Volcanol Geotherm Res 2015;300:129–47. doi:`10.1016/j.jvolgeores.2014.12.015`. `arXiv:1405.0883`.

Chacón Rebollo T, Lewandowski R. Mathematical and numerical foundations of turbulence models. Birkhäuser, New-York, 2013.

Chai X, Mahesh K. Dynamic k-equation model for large-eddy simulation of compressible flows. J Fluid Mech 2012;699(July):385–413.

Costa A, Folch A, Macedonio G. Density-driven transport in the umbrella region of volcanic clouds: Implications for tephra dispersion models. Geophys Res Lett 2013;40(18):4823–7. doi:`10.1002/grl.50942`.

Costa A, Macedonio G, Folch A. A three-dimensional Eulerian model for transport and deposition of volcanic ashes. Earth Planet Sci Lett 2006;241(3-4):634–47. doi:`10.1016/j.epsl.2005.11.019`.

Costa A, Suzuki YJ, Cerminara M, Devenish BJ, Esposti Ongaro T, Herzog M, Van Eaton AR, Denby L, Bursik MI, de' Michieli Vitturi M, Engwell S, Neri A, Barsotti S, Folch A, Macedonio G, Girault F, Carazzo G, Tait S, Kaminski E, Mastin LG, Woodhouse MJ, Phillips JC, Hogg AJ, Degruyter W, Bonadonna C. Results of the eruptive column model inter-comparison study. J Volcanol Geotherm Res 2016;doi:`10.1016/j.jvolgeores.2016.01.017`; in press.

de' Michieli Vitturi M, Engwell S, Neri A, Barsotti S. Uncertainty quantification and sensitivity analysis of volcanic columns models: results from the integral model PLUME-MoM. J Volcanol Geotherm Res 2016;doi:`10.1016/j.jvolgeores.2016.03.014`; from Duplicate 2 (Uncertainty quantification and sensitivity analysis of volcanic columns models: results from the integral model PLUME-MoM - de' Michieli Vitturi, Mattia; Engwell, Samantha; Neri, Augusto; Barsotti, S.) Accepted.

Dobran F, Neri A, Macedonio G. Numerical simulation of collapsing volcanic columns. J Geophys Res 1993;98(B3):4231–59.

Elghobashi S. Particle-laden turbulent flows: direct simulation and closure models. Appl Sci Res 1991;48(3-4):301–14.

Elghobashi S. On predicting particle-laden turbulent flows. Appl Sci Res 1994;52(4):309–29.

Erlebacher G, Hussaini MY, Speziale CG, Zang TA. Toward the large-eddy simulation of compressible turbulent flows. ICASE Report 90-76. Technical Report; ICASE/NASA Langley Research Center; 1990.

Esposti Ongaro T, Cerminara M. Non-equilibrium processes in ash-laden volcanic plumes: new insights from 3D multiphase flow simulations. J Volcanol Geotherm Res 2016;doi:`10.1016/j.jvolgeores.2016.04.004`; in press.

Esposti Ongaro T, Neri A, Menconi G, de' Michieli Vitturi M, Marianelli P, Cavazzoni C, Erbacci G, Baxter PJ. Transient 3D numerical simulations of column collapse and pyroclastic density current scenarios at Vesuvius. J Volcanol Geotherm Res 2008;178(3):378–96.

Ferry J, Balachandar S. A fast Eulerian method for disperse two-phase flow. Int J Multiph flow 2001;27:1199–226.

Ferry J, Balachandar S. Equilibrium Eulerian approach for predicting the thermal field of a dispersion of small particles. Int J Heat Mass Transf 2005;48(3):681–9. doi:`10.1016/j.ijheatmasstransfer.2004.07.047`.

Ferry J, Rani SL, Balachandar S. A locally implicit improvement of the equilibrium Eulerian method. Int J Multiph Flow 2003;29(6):869–91. doi:`10.1016/S0301-9322(03)00064-8`.

Ferziger JH, Perić M. Computational methods for fluid dynamics. volume 3. Springer Berlin, 1996.

Fureby C. On subgrid scale modeling in large eddy simulations of compressible fluid flow. Phys Fluids 1996;8(5):1301. doi:`10.1063/1.868900`.

Garnier E, Adams N, Sagaut P. Large Eddy Simulation for Compressible Flows. Scientific Computation. Dordrecht: Springer Netherlands, 2009. doi:`10.1007/978-90-481-2819-8`.

Herzog M, Graf HF. Applying the three-dimensional model ATHAM to volcanic plumes: Dynamic of large co-ignimbrite eruptions and associated injection heights for volcanic gases. Geophys Res Lett 2010;37(19):1–5. doi:`10.1029/2010GL044986`.

Holasek RE, Self S, Woods AW. Satellite observations and interpretation of the 1991 Mount Pinatubo eruption plumes. J Geophys Res 1996;101(B12):27635–55. doi:`10.1029/96JB01179`.

Issa RI. Solution of the implicitly discretised fluid flow equations by operator-splitting. J Comput Phys 1986;62(1):40–65. doi:`10.1016/0021-9991(86)90099-9`.

Johnson JB, Ripepe M. Volcano infrasound: A review. J Volcanol Geotherm Res 2011;206(3-4):61–9. doi:`10.1016/j.jvolgeores.2011.06.006`.

Kaminski É, Tait S, Carazzo G. Turbulent entrainment in jets with arbitrary buoyancy. J Fluid Mech 2005;526:361–76. doi:`10.1017/S0022112004003209`.

Lesieur M, Métais O, Comte P. Large-Eddy Simulations of Turbulence. volume 1. Cambridge University Press, 2005.

Lodato G, Vervisch L, Domingo P. A compressible wall-adapting similarity mixed model for large-eddy simulation of the impinging round jet. Phys Fluids 2009;21(3):035102. doi:`10.1063/1.3068761`.

Marble FE. Dynamics of Dusty Gases. Annu Rev Fluid Mech 1970;2(1):397–446. doi:`10.1146/annurev.fl.02.010170.002145`.

Mathew J, Basu AJ. Some characteristics of entrainment at a cylindrical turbulence boundary. Phys Fluids 2002;14(7):2065. doi:`10.1063/1.1480831`.

Matoza RS, Fee D, Garcés MA, Seiner JM, Ramón PA, Hedlin MAH. Infrasonic jet noise from volcanic eruptions. Geophys Res Lett 2009;36(8):L08303. doi:`10.1029/2008gl036486`.

Moin P, Squires KD, Cabot WH, Lee S. A dynamic subgrid-scale model for compressible turbulence and scalar transport. Phys Fluids A 1991;3(11):2746. doi:`10.1063/1.858164`.

Morton BR, Taylor G, Turner JS. Turbulent Gravitational Convection from Maintained and Instantaneous Sources. Proc R Soc A Math Phys Eng Sci 1956;234(1196):1–23. doi:`10.1098/rspa.1956.0011`.

Neri A, Dobran F. Influence of eruption parameters on the thermofluid dynamics of collapsing volcanic columns. J Geophys Res 1994;99(B6):11833–57. doi:`10.1029/94JB00471`.

Nicoud F, Ducros F. Subgrid-scale stress modelling based on the square of the velocity gradient tensor. Flow, Turbul Combust 1999;62(3):183–200. doi:`10.1023/A:1009995426001`.

Piscaglia F, Montorfano A, Onorati A. Towards the LES Simulation of IC Engines with Parallel Topologically Changing Meshes. SAE Int J Engines 2013;6(2):926–40. doi:`10.4271/2013-01-1096`.

Plourde F, Pham MV, Kim SD, Balachandar S. Direct numerical simulations of a rapidly expanding thermal plume: structure and entrainment interaction. J Fluid Mech 2008;604:99–123. doi:`10.1017/S0022112008001006`.

Pope SB. Turbulent flows. Cambridge university press, 2000.

Ricou FP, Spalding DB. Measurements of entrainment by axisymmetrical turbulent jets. J Fluid Mech 1961;11(01):21. doi:`10.1017/S0022112061000834`.

da Silva CB, Hunt JC, Eames I, Westerweel J. Interfacial Layers Between Regions of Different Turbulence Intensity. Annu Rev Fluid Mech 2014;46(1):567–90. doi:`10.1146/annurev-fluid-010313-141357`.

Sparks RSJ. The dimensions and dynamics of volcanic eruption columns. Bull Volcanol 1986;48:3–15.

Sparks RSJ, Bursik MI, Carey S, Gilbert J, Glaze LS, Sigurdsson H, Woods AW. Volcanic Plumes. John Wiley & Sons, Inc., 1997.

Suzuki YJ, Costa A, Cerminara M, Esposti Ongaro T, Herzog M, Van Eaton AR, Denby L. Inter-comparison of three-dimensional models of volcanic plumes. J Volcanol Geotherm Res 2016;Submitted.

Suzuki YJ, Koyaguchi T. A three-dimensional numerical simulation of spreading umbrella clouds. J Geophys Res 2009;114(October 2008):1–18. doi:`10.1029/2007JB005369`.

Suzuki YJ, Koyaguchi T. Numerical determination of the efficiency of entrainment in volcanic eruption columns. Geophys Res Lett 2010;37(5):L05302. doi:`10.1029/2009GL042159`.

Suzuki YJ, Koyaguchi T. 3-D numerical simulations of eruption column collapse: Effects of vent size on pressure-balanced jet/plumes. J Volcanol Geotherm Res 2012;221-222:1–13. doi:`10.1016/j.jvolgeores.2012.01.013`.

Suzuki YJ, Koyaguchi T. 3D numerical simulation of volcanic eruption clouds during the 2011 Shinmoe-dake eruptions. Earth, Planets Sp 2013;65(6):581–9. doi:`10.5047/eps.2013.03.009`.

Suzuki YJ, Koyaguchi T. Effects of wind on entrainment efficiency in volcanic plumes. J Geophys Res Solid Earth 2015;120(9):6122–40. doi:`10.1002/2015JB012208`.

Suzuki YJ, Koyaguchi T, Ogawa M, Hachisu I. A numerical study of turbulent mixing in eruption clouds using a three-dimensional fluid dynamics model. J Geophys Res 2005;110(B8):B08201. doi:`10.1029/2004JB003460`.

Tam CKW, Golebiowski M, Seiner JM. On the two components of turbulent mixing noise from supersonic jets. AIAA J 1996;96-1716:18.

Taveira RMR, da Silva CB, Pereira JCF. The Dynamics of Turbulent Scalar Mixing near the Edge of a Shear Layer. J Phys Conf Ser 2011;318:052049. doi:`10.1088/1742-6596/318/5/052049`.

Toschi F, Bodenschatz E. Lagrangian Properties of Particles in Turbulence. Annu Rev Fluid Mech 2009;41(1):375–404. doi:`10.1146/annurev.fluid.010908.165210`.

Townsend AA. The mechanism of entrainment in free turbulent flows. J Fluid Mech 1966;26(689).

Van Eaton AR, Mastin LG, Herzog M, Schwaiger HF, Schneider DJ, Wallace KL, Clarke AB. Hail formation triggers rapid ash aggregation in volcanic plumes. Nat Commun 2015;6:7860. doi:`10.1038/ncomms8860`.

Vreman B, Geurts BJ, Kuerten H. A priori tests of large eddy simulation of the compressible plane mixing layer. J Eng Math 1995;29(4):299–327. doi:`10.1007/BF00042759`.

Vuorinen V, Yu J, Tirunagari S, Kaario O, Larmi M, Duwig C, Boersma BJ. Large-eddy simulation of highly underexpanded transient gas jets. Phys Fluids 2013;25(1):1–22. doi:`10.1063/1.4772192`.

Westerweel J, Fukushima C, Pedersen JM, Hunt JC. Mechanics of the turbulent-nonturbulent interface of a jet. Phys Rev Lett 2005;95(17):1–4. doi:`10.1103/PhysRevLett.95.174501`.

Wilson L, Sparks RSJ, Huang T, Watkins ND. The control of volcanic column heights by eruption energetics and dynamics. J Geophys Res 1978;83(B4):1829. doi:`10.1029/JB083iB04p01829`.

Wilson L, Sparks RSJ, Walker GPL. Explosive volcanic eruptionsIV. The control of magma properties and conduit geometry on eruption column behaviour. Geophys J R Astron Soc 1980;63(1):117–48.

Woods AW. The fluid dynamics and thermodynamics of eruption columns. Bull Volcanol 1988;50(3):169–93.

Woods AW. Turbulent Plumes in Nature. Annu Rev Fluid Mech 2010;42(1):391–412. doi:`10.1146/annurev-fluid-121108-145430`.

Yoshizawa A. Bridging between eddy-viscosity-type and second-order turbulence models through a two-scale turbulence theory. Phys Rev E 1993;48(1):273–81. doi:`10.1103/PhysRevE.48.273`.

Zhou X, Luo KH, Williams JJR. Large-eddy simulation of a turbulent forced plume. Eur J Mech B/Fluids 2001;20(2):233–54. doi:`10.1016/S0997-7546(00)01117-1`.